Biomechanical Modeling of Paralympic Wheelchair Curling

by

Brock Laschowski

A thesis

presented to the University of Waterloo

in fulfillment of the

thesis requirement for the degree of

Master of Applied Science

in

Mechanical Engineering

Waterloo, Ontario, Canada, 2016

Author's Declaration

I hereby declare that I am the sole author of this thesis. This is a true copy of the thesis, including any required final revisions, as accepted by my examiners. I understand that my thesis may be made electronically available to the public.

Abstract

This research represents the first documented investigation into the biomechanics and neural motor control of Paralympic wheelchair curling. A multibody biomechanical model of the wheelchair curling delivery was developed in reference to a Team Canada Paralympic athlete with a spinal cord injury. Subject-specific body segment parameters were quantified via dual-energy x-ray absorptiometry. The angular joint kinematics throughout the wheelchair curling delivery were experimentally measured using an inertial measurement unit system; the translational kinematics of the curling stone were additionally evaluated with optical motion capture. The experimental kinematics were optimized to satisfy the kinematic constraints of the multibody biomechanical model. The optimized kinematics were subsequently used to compute the resultant joint moments through inverse dynamics analysis. The neural motor control of the Paralympic athlete was modeled using forward dynamic optimization. The predicted kinematics from different optimization objective functions were compared with those experimentally measured throughout the wheelchair curling delivery. Of the optimization objective functions under consideration, minimizing angular joint accelerations resulted in the most accurate predictions of the kinematic trajectories and the shortest optimization computation time. The implications of these findings are discussed in relation to musculoskeletal modeling and optimal equipment design through predictive simulation.

Acknowledgments

I want to thank:

- Dr. John McPhee, my MASc Supervisor and Director of the Motion Research Group
- Dr. Naser Mehrabi, Postdoctoral Fellow in the Motion Research Group
- Dr. James Tung, Professor of Mechanical Engineering at the University of Waterloo
- Dr. Steven Dilkas, Medical Physician at the Canadian Sport Institute Ontario
- Dr. Heather Sprenger, Research Lead at the Canadian Sport Institute Ontario
- Members of the Canadian Paralympic Wheelchair Curling Team
- Members of the Motion Research Group at the University of Waterloo
- Katherine Cornacchia, my Fiancé

Table of Contents

List of Figures

List of Tables

1 Introduction

1.1 Paralympic Games

The notion of Paralympic sport originated from Ludwig Guttmann in the late 1940s (Vanlandewijck and Thompson, 2011). As Director of the National Spinal Injuries Unit at the Stoke Mandeville Hospital in England, Guttmann prescribed competitive wheelchair activities as a method of physical rehabilitation for individuals with spinal cord injuries. Guttmann's provisional wheelchair competitions eventually developed into what is now the Paralympic Games. The first Summer Paralympic Games were in 1960 and the first Winter Paralympic Games were in 1976 (Vanlandewijck and Thompson, 2011). The International Paralympic Committee, established in 1989, oversees both the Summer and Winter Paralympic Games. There are currently 20 summer Paralympic sports and 4 winter Paralympic sports. A wide variety of individuals are eligible to compete at the Paralympic Games, including those with spinal cord injuries, visual impairments, lower and upper extremity amputations, cerebral palsy, and "les autres" (Keogh, 2011). As a testament to its increasing popularity, approximately 4000 athletes from over 146 countries competed at the 2008 Paralympic Games (Keogh, 2011).

1.2 Sports Biomechanics

There has been limited research published regarding the biomechanics of Paralympic sports. Biomechanics is the quantitative analysis of multibody human movements using principles of mechanics, and can be subcategorized into kinematics and dynamics. Kinematics describes human movements (e.g., displacements, velocities, and

accelerations) without reference to its causes, and dynamics describes the forces and moments that illicit multibody movements. The human musculoskeletal system is exceptionally complex, with over 206 bones and 640 skeletal muscles (Zatsiorsky, 1998). Consequently, biomechanists frequently evaluate the kinematics and dynamics of multibody human movements using computational engineering methods like optimization, mathematical modelling, control theory, multibody system dynamics, and computer simulation.

The majority of the Paralympic sports biomechanics research has been limited to experimental methods (Keogh, 2011). Moreover, these investigations have primarily focused on summer Paralympic sports, specifically i) wheelchair propulsion in wheelchair basketball (Mason et al, 2013) and wheelchair rugby (Usma-Alvarez et al, 2014), and ii) sprint biomechanics of track and field athletes with lower extremity prosthetics (Hobara et al, 2016; Weyand et al, 2009). Accordingly, little is known regarding the biomechanics of winter Paralympic sports (e.g., wheelchair curling).

1.3 Wheelchair Curling

Wheelchair curling debuted at the 2006 Paralympic Games. Competing athletes utilize the same stones and ice sheets as Olympic curlers, although sweeping (i.e., using a broom to control the stone's trajectory) is omitted and the stone must be delivered from a stationary wheelchair using a delivery stick (World Curling Federation, 2014). Figure 1.1 presents a standard curling ice sheet. The stone must be released from the delivery stick before crossing the hog line. The linear distance between the hog line and the geometrical center of the button located at the opposite end of the ice sheet (i.e., the intersection between the center and tee lines) is 28.35 m. Similar to Olympic curling

(Yoo et al, 2012), the objective in wheelchair curling is to position one or more stones within the targeted area (i.e., the house) nearby the geometric center (i.e., the button) in order to accumulate points and to displace the opposition's stones from the scoring area. Research conducted at the 2010 Paralympic Games noted that 18 % of athletes competing in wheelchair curling (n = 50) sought medical attention for musculoskeletal injuries, the majority of which were sustained about the lower back and upper extremity joints (Webborn et al, 2012).

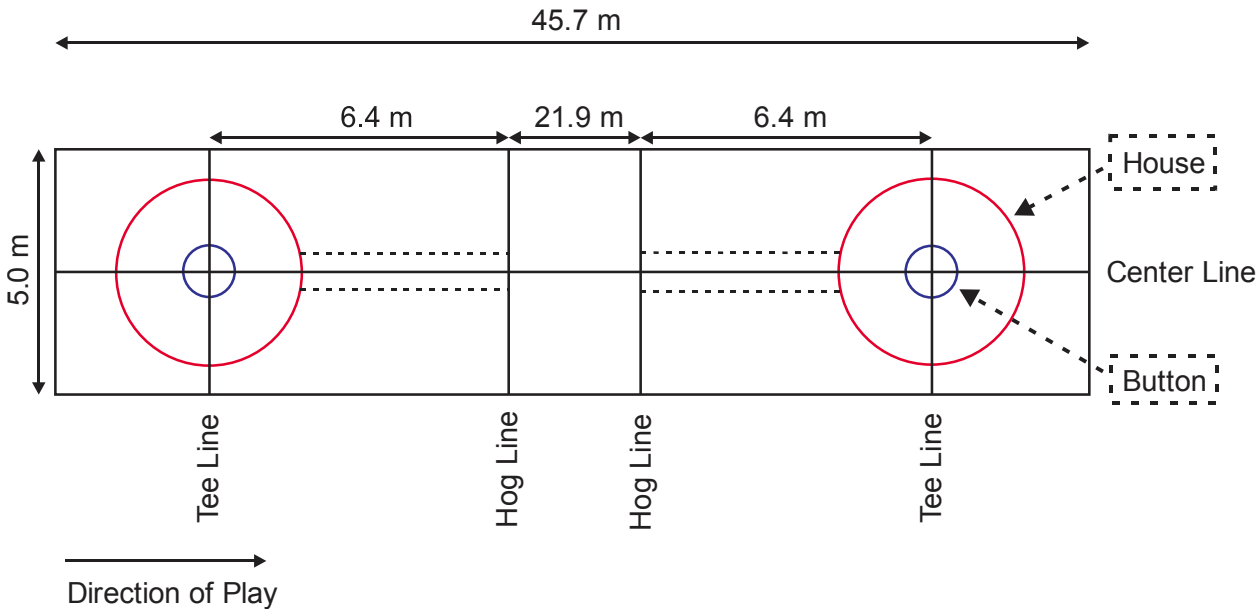

Figure 1.1. Schematic of a standard curling ice sheet.

1.4 Contributions and Organization of Thesis

To the best of the author's knowledge, there has been no experimental or computational research published regarding the biomechanics of wheelchair curling. These investigations would provide unprecedented insights into the physical demands of this Paralympic sport. Accordingly, the objectives of this research were i) to design a novel multibody biomechanical model of a Paralympic wheelchair curler using subject-

specific body segment parameters (Chapter 2), ii) to quantitatively evaluate the joint kinematics and dynamics throughout the wheelchair curling delivery via experimental measurements and inverse dynamics analysis (Chapter 3), and iii) to predict the neural motor control employed by the Paralympic wheelchair curler using forward dynamic optimization (Chapter 4).

1.5 Paralympic Athlete

A single wheelchair curler (sex = male, age = 39 years) was recruited from the Canadian Paralympic Team. The athlete was a gold medalist at the 2014 Paralympic Games and 2013 World Wheelchair Curling Championships. In 2007, the athlete was involved in a helicopter accident and sustained a traumatic incomplete spinal cord injury between the 5^{th} and 6^{th} cervical vertebrae. An incomplete spinal cord injury involves preservation of sensory and/or motor function below the neurological level of injury (Kirshblum et al, 2011). The Paralympian has significant paralysis in his right hand. In order to deliver the curling stone with a sufficient amount of propulsive force, the Paralympian developed a custom-made grasping handle, affixed to the end of the delivery stick.

The athlete was diagnosed with a level "*C*" impairment on the American Spinal Injury Association (ASIA) Impairment Scale. The ASIA Impairment Scale is an internationally recognized method of categorizing motor and sensory impairments in individuals with spinal cord injuries. The scores range between "*A*" and "*E*", wherein *A* represents a complete spinal cord injury and *E* represents normal sensory and motor function. The Paralympian provided informed written consent, and the Canadian Sport Institute Ontario Research Ethics Board (Appendix 1) and the University of Waterloo Office of Research Ethics (Appendix 2) approved this research.

2 Multibody Biomechanical Model

2.1 Body Segment Parameters

2.1.1 Cadaveric Research

The human body can be modeled as a multibody system whereby each body segment can be characterized by specific mechanical parameters (i.e., mass, length, position vector of the center of mass, and principal mass moment of inertia), as illustrated in Figure 2.1. The cadaveric research by Clauser et al (1969) and Dempster (1955) comprise two of the most renowned investigations for determining human body segment parameters. These investigations presented a number of anthropometric percentages for each body segment, including i) the position vector of the center of mass as a percentage of the segment's length, ii) the segment's mass as a percentage of the subject's total body mass, and iii) the radius of gyration about the center of mass as a percentage of the segment's length. Clauser et al (1969) and Dempster (1955) focused exclusively on able-bodied individuals (i.e., Clauser et al (1969): n = 13 cadavers, age = 49 ± 13 years, supine height = 1.73 ± 0.06 m, total body mass = 66.52 ± 8.70 kg; Dempster (1955): n = 8 cadavers, age = 69 ± 11 years, supine height = 1.69 ± 0.11 m, total body mass = 59.53 ± 8.32 kg).

Recent multibody biomechanical models of manual wheelchair users (Morrow et al, 2014; Rankin et al, 2012; Slowik and Neptune, 2013) have utilized the anthropometric percentages by Clauser et al (1969) and Dempster (1955) to represent the body segment parameters of individuals with spinal cord injuries. Nevertheless, it has been well documented that individuals with spinal cord injuries have less skeletal muscle mass

(Kocina, 1997; Sutton et al, 2009), lower bone mineral content (Kocina, 1997), and more adipose tissue (Sutton et al, 2009) in the lower extremities than able-bodied matched controls. Several studies have also reported higher skeletal muscle mass in the upper extremities of individuals with spinal cord injuries compared with able-bodied equivalents (Bulbulian et al, 1987). Accordingly, the validity of using the anthropometric percentages by Clauser et al (1969) and Dempster (1955) to represent the body segment parameters of individuals with spinal cord injuries (i.e., similar to the methods used by Morrow et al (2014), Rankin et al (2012), and Slowik and Neptune (2013)) is questionable.

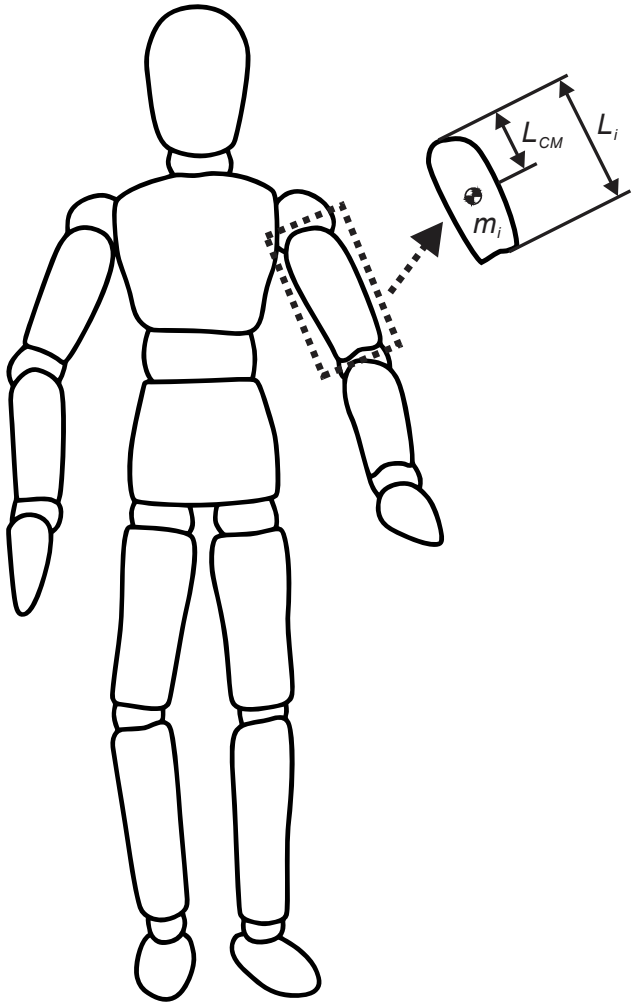

Figure 2.1. Body segment parameters of a multibody biomechanical model.

2.1.2 Dual-Energy X-Ray Absorptiometry

Medical imaging technologies like computed tomography (CT) and magnetic resonance imaging (MRI) have been used to measure *in vivo* the body segment parameters of living subjects (Keil et al, 2016). Nevertheless, these methods are time-consuming and expensive, and involve large doses of ionizing radiation in the case of CT imaging (i.e., 10,000-15,000 μSv per total body scan) (Keil et al, 2016). An emerging medical imaging technology is dual-energy x-ray absorptiometry (DXA). Compared with CT and MRI, DXA imaging is faster, more accessible, inexpensive, simple to operate, and involves minimal doses of radiation (Durkin et al, 2002; Durkin and Dowling, 2003). Moreover, DXA imaging is not enclosed, which minimizes the likelihood of the subject feeling claustrophobic.

Previous research has used DXA imaging to measure the body compositions of individuals with spinal cord injuries (Goktepe et al, 2004; Inukai et al, 2006; Mojtahedi et al, 2009). Nonetheless, these investigations were limited to recreationally active individuals and/or did not include segmental analyses (i.e., only total body measurements were reported). The body segment parameters of the Paralympic wheelchair curler were experimentally measured using DXA imaging. Total body DXA scans were conducted at the Canadian Sport Institute Ontario using a Lunar iDXA (Figure 2.2).

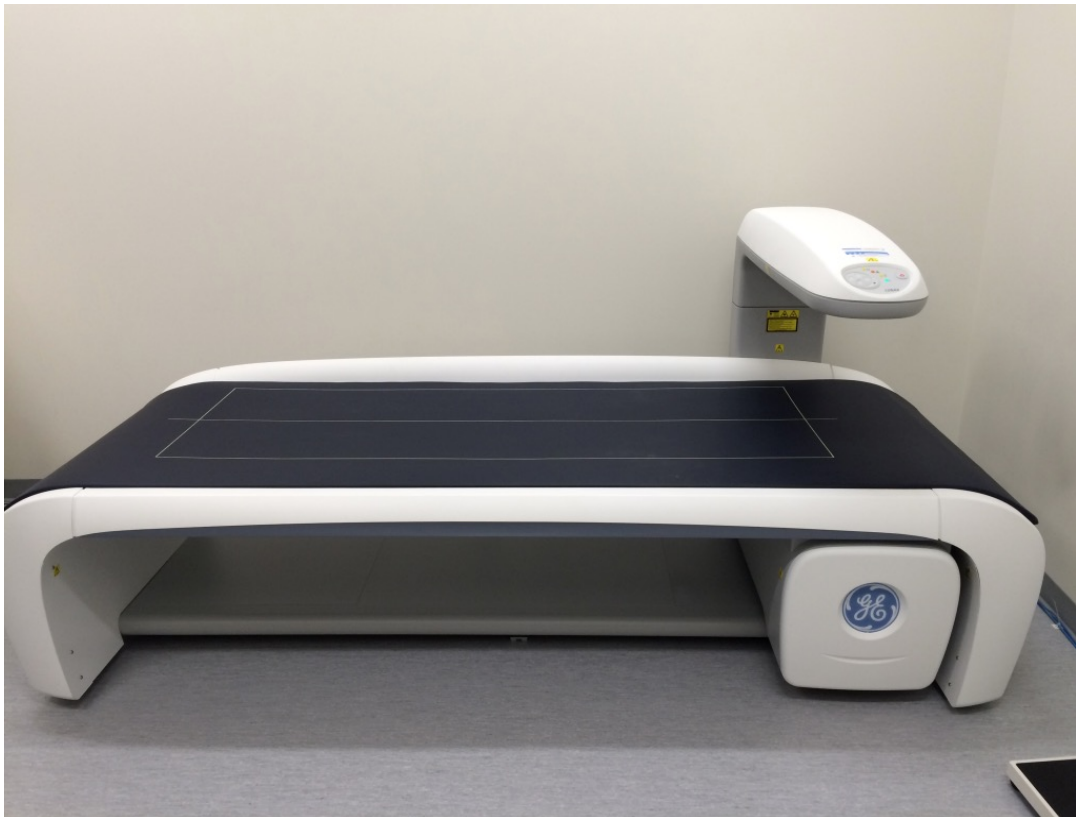

Figure 2.2. Photograph of the DXA instrumentation.

The DXA instrumentation emits a narrow angled, fan-beam x-ray filtered at two levels of energy: 41 and 74 keV (GE Healthcare Lunar, 2013). As the beam passes through the Paralympian's body, the photons are attenuated through Compton scattering and photoelectric absorption, and the emerging energy levels are diminished (Durkin et al, 2002). Based on the beam's attenuation, percentages of adipose tissue, bone mineral content, and lean soft tissue (e.g., skeletal muscle) are determined by the DXA instrumentation on a pixel-by-pixel basis. The mass of each pixel is subsequently computed assuming set densities for each tissue (GE Healthcare Lunar, 2013).

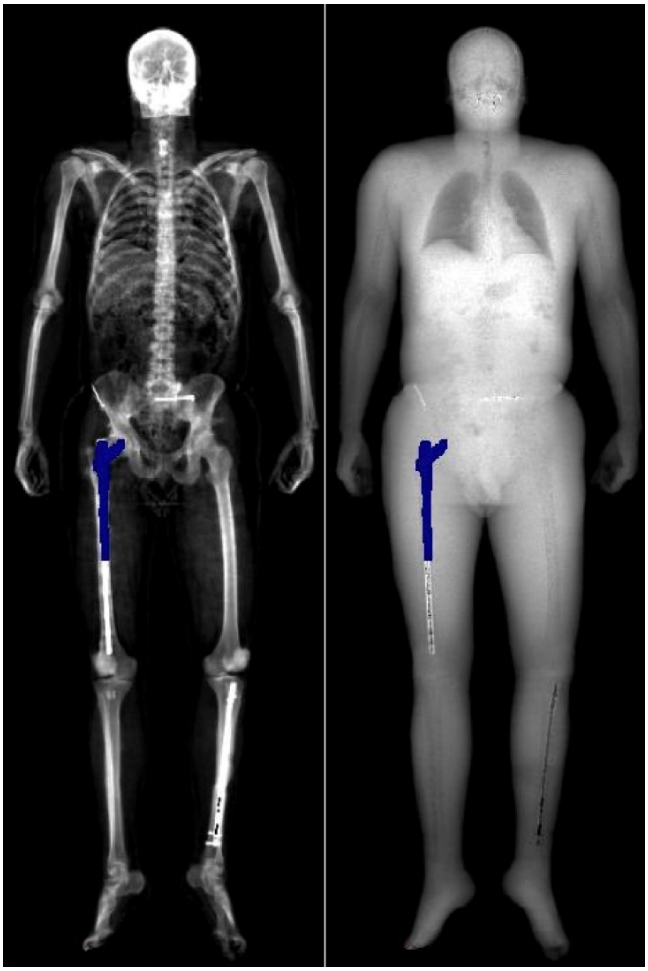

Figure 2.3. Total body DXA images of the Paralympic athlete in the frontal plane.

The Paralympian fasted for 12 hours (i.e., no food and fluids) and abstained from physical activity and calcium supplementation for 24 hours prior to the DXA imaging. The DXA instrumentation was calibrated against a criterion phantom block (GE Healthcare Lunar, 2013). The athlete wore compression undergarments, removed all jewellery, and voided his bladder before the DXA imaging. A medical radiation technologist laid the Paralympian supine in the anatomical position on the DXA table. The athlete underwent two total body DXA scans and was repositioned between scans. Each scan took approximately 7 minutes to complete and had an effective dose of

radiation of 0.96 μSv (GE Healthcare Lunar, 2013). Data were analyzed with enCORE version 15 software (GE Medical Systems Ultrasound and Primary Care Diagnostics, USA). The DXA instrumentation reconstructs two-dimensional images in the frontal plane, as illustrated in Figure 2.3; the image on the left displays the skeleton and the image on the right includes the soft tissue.

Each total body DXA image was manually delineated into fourteen segments: head-and-neck, torso, and right and left upper arms, forearms, hands, thighs, shanks, and feet. Similar proximal and distal endpoints used by Clauser et al (1969) and Dempster (1955) were used to delineate each body segment in the total body DXA images. It was important to investigate whether the body segment parameters experimentally measured through the DXA imaging differed from the anthropometric percentages offered by Clauser et al (1969) and Dempster (1955). If the quantities were relatively similar, it might suffice to simply use the cadaveric approximations to characterize the body segment parameters of the Paralympic athlete. The mass of each body segment as a percentage of the Paralympian's total body mass (P_{m_i}) was calculated by

$$P_{m_i} = \frac{m_i}{m_{total}} 100 \quad (1)$$

where m_i is the mass of a given body segment and m_{total} is the Paralympian's total body mass, both of which were experimentally measured using the DXA imaging. The experimental P_{m_i} were compared with the mass percentages (P'_{m_i}) reported by Clauser et al (1969) and Dempster (1955). The cadaveric investigations measured the mass of each body segment with gauges accurate to 0.001 kg. The sums of the P'_{m_i} by Clauser et al

(1969) and Dempster (1955) equate to 99.9 % and 95.3 %, respectively. These undervaluations were attributed to fluid and tissue losses sustained during the cadaver dissections.

Table 2.1 presents the experimental P_{m_i} from the DXA imaging and the P'_{m_i} reported by Clauser et al (1969) and Dempster (1955). Dempster (1955) provided quantities for both extremities whereas Clauser et al (1969) reported only arithmetic means. The uncertainties in the P'_{m_i} represent inter-cadaver differences. Compared with the experimental P_{m_i} from the DXA imaging, the P'_{m_i} were lower for the head-and-neck, torso, right upper arm, left upper arm, and left thigh segments by 5.7 %, 3.8 %, 24.1 %, 26.7 %, and 6.1 %, respectively (Laschowski and McPhee, 2016a). In contrast, the P'_{m_i} were higher for the right hand, left hand, right thigh, right shank, left shank, right foot, and left foot segments by 46.3 %, 40.1 %, 4.4 %, 12.7 %, 20.3 %, 20.8 %, and 30.7 %, respectively (Laschowski and McPhee, 2016a).

Table 2.1. Mass of each body segment as a percentage of the Paralympian's total body mass i) as measured via the DXA imaging and ii) as approximated by Clauser et al (1969) and Dempster (1955).

Body Segment	DXA Imaging (%)	Clauser et al (%)	Dempster (%)
Head & Neck	7.9 ± 0.1	7.3 ± 0.6	7.6 ± 0.9
Torso	50.8 ± 0.2	50.7 ± 2.1	46.9 ± 2.8
Upper Arm (R / L)	3.5 ± 0.3 / 3.5 ± 0.2	2.6 ± 0.2	2.7 ± 0.3 / 2.6 ± 0.3
Forearm (R / L)	1.6 ± 0.1 / 1.5 ± 0.1	1.6 ± 0.2	1.6 ± 0.2 / 1.5 ± 0.1
Hand (R / L)	0.5 ± 0.1 / 0.5 ± 0.1	0.7 ± 0.1	0.6 ± 0.1 / 0.7 ± 0.1
Thigh (R / L)	9.5 ± 0.6 / 10.7 ± 0.3	10.3 ± 0.8	9.6 ± 1.5 / 9.7 ± 1.8
Shank (R / L)	4.0 ± 0.1 / 3.7 ± 0.1	4.4 ± 0.4	4.5 ± 0.6 / 4.5 ± 0.6
Foot (R / L)	1.2 ± 0.1 / 1.2 ± 0.1	1.5 ± 0.1	1.4 ± 0.1 / 1.5 ± 0.2

Previous research (Andrews and Mish, 1996; Kingma et al, 1996; Rao et al, 2006) has demonstrated that differences in body segment parameters (i.e., particularly the mass parameter) can significantly affect the resultant joint moments during inverse dynamics analysis. The observed differences between the DXA measurements and cadaveric approximations support the implementation of using DXA imaging to experimentally quantify the body segment parameters of the Paralympic athlete in the interests of developing a valid multibody biomechanical model of wheelchair curling. Similar differences in body segment masses between the DXA measurements and cadaveric approximations were observed with the total Canadian Paralympic Wheelchair Curling Team (Appendix 3).

2.2 Design of Biomechanical Model

A novel biomechanical model of the wheelchair curling delivery was developed in MapleSim (MapleSoft, Canada). The model consists of a two-dimensional multibody slider mechanism with a closed kinematic chain (Figure 2.4).

2.2.1 Rigid Body Segments

Body T is the torso, body H&N is the head-and-neck, body UA is the right upper arm, body FA is the right forearm, body HD is the right hand, body DS is the delivery stick, and body S is the curling stone. Each segment is modelled as a rigid body. The wheelchair is fixed to an inertial XY reference frame. Table 2.2 displays the length and mass parameters of each biological body segment as experimentally measured using the DXA imaging (Laschowski and McPhee, 2016b). The measurements are presented as

arithmetic means over consecutive DXA scans with uncertainties expressed as ± 1 standard deviation.

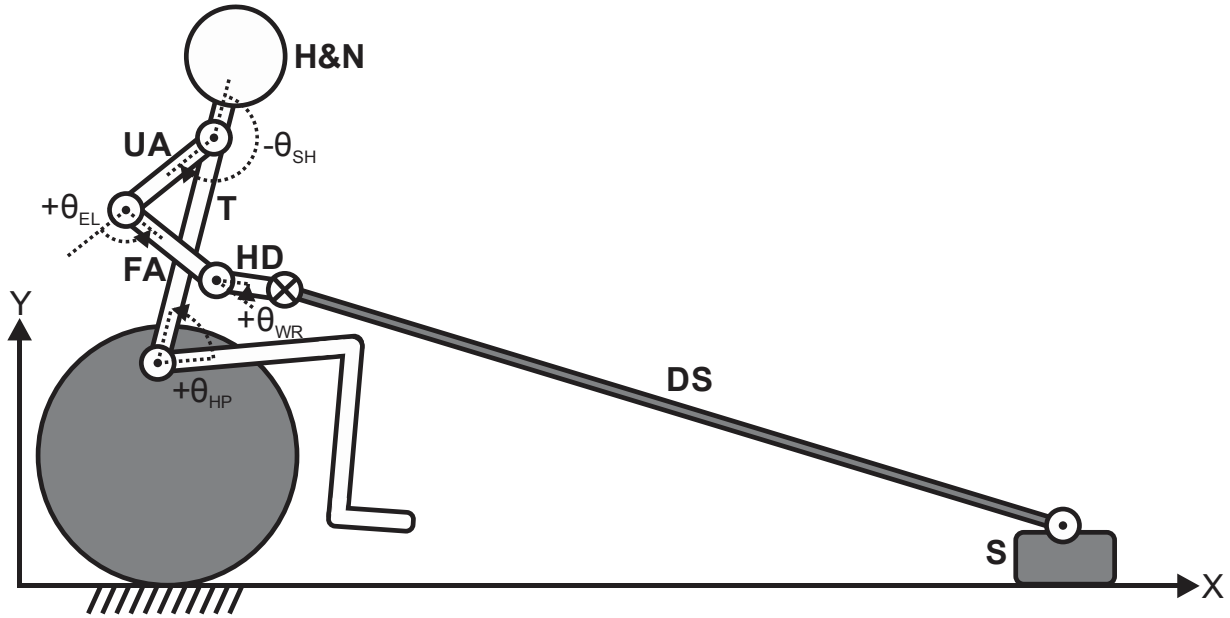

Figure 2.4. Schematic of the multibody biomechanical model of wheelchair curling.

The segment lengths in Table 2.2 represent the linear distances between the proximal and distal endpoints. The measurements had a high degree of test-retest reliability, as indicated by the small standard deviations. Altogether, the length measurements differed by 2.8 % ± 2.4 percentage points (pp) between parallel body segments in the right and left extremities. Table 2.2 also shows the mass (m_i) of each body segment as experimentally measured using the DXA imaging. In general, the m_i differed by 6.7 % ± 4.8 pp between corresponding body segments in the right and left extremities. The largest asymmetrical difference was measured between the two thigh segments (i.e., up to 20.1 %). This difference can be explained by the fact that the Paralympian has a titanium intramedullary implant in the right femur. Whenever the DXA beam is radiated against a metallic implant, insufficient amounts of data transmit

through to the DXA receiver and the mass of that area cannot be quantified (i.e., its value is set to zero). The lower m_i of the right thigh segment, relative to the left side, can be attributed to the high photon attenuation in the pixels coinciding with the femoral intramedullary implant. Summing the m_i of each body segment resulted in an estimated total body mass of 87.88 ± 0.96 kg.

Table 2.2. Length (m) and mass (kg) of each body segment of the Paralympic athlete. The quantities are presented as arithmetic means ± 1 standard deviation across multiple DXA scans. Segments in the extremities are subcategorized into right and left sides.

Body Segment	Length (m ± 1 SD)	Mass (kg ± 1 SD)
Head & Neck	0.265 ± 0.005	6.967 ± 0.085
Torso	0.588 ± 0.008	44.616 ± 0.677
Upper Arm (R / L)	0.291 ± 0.005 / 0.290 ± 0.001	3.099 ± 0.192 / 3.100 ± 0.035
Forearm (R / L)	0.276 ± 0.002 / 0.280 ± 0.007	1.371 ± 0.009 / 1.302 ± 0.027
Hand (R / L)	0.123 ± 0.001 / 0.117 ± 0.002	0.396 ± 0.011 / 0.437 ± 0.013
Thigh (R / L)	0.469 ± 0.003 / 0.464 ± 0.004	8.383 ± 0.629 / 9.396 ± 0.201
Shank (R / L)	0.398 ± 0.001 / 0.400 ± 0.001	3.482 ± 0.034 / 3.261 ± 0.071
Foot (R / L)	0.178 ± 0.003 / 0.187 ± 0.003	1.039 ± 0.008 / 1.037 ± 0.039

There is presently insufficient evidence to suggest that the position vector of the center of mass and principal mass moment of inertia of a given body segment significantly differ between individuals with spinal cord injuries and able-bodied matched controls. Consequently, the position vector of the center of mass from the proximal endpoint (r_{CM_i}) and the principal mass moment of inertia about the center of mass (I_{CM_i}) can be mathematically approximated via

$$r_{CM_i} = P'_{r_{CM_i}} L_i \tag{2}$$

$$I_{CM_i} = m_i \left(P'_{k_{CM_i}} L_i \right)^2 \quad (3)$$

where L_i is the segment's length as experimentally measured via the DXA imaging, $P'_{r_{CM_i}}$ is the position vector of the center of mass from the proximal endpoint as a proportion of L_i, and $P'_{k_{CM_i}}$ is the radius of gyration about the center of mass as a proportion of L_i. The latter two terms were obtained from Clauser et al (1969). The proximal and distal endpoints and the r_{CM_i} were assumed to be located along the segment's midline in the medial-lateral axis. Table 2.3 presents the r_{CM_i} and I_{CM_i} of each body segment in the frontal plane (Laschowski and McPhee, 2016b). These body segment parameters, coupled with the mass and length measurements from Table 2.2, were used to design the multibody biomechanical model. Independent of the population being evaluated, future research should consider quantifying the r_{CM_i} and I_{CM_i} in other planes using digital image processing algorithms (Lee et al, 2009).

Table 2.3. Position vector of the center of mass (m) and principal mass moment of inertia about the center of mass (kg·m^2) of each body segment as calculated via equations (2) and (3), respectively.

Body Segment	Center of Mass (m ± 1 SD)	Mass Moment of Inertia (kg·m^2 ± 1 SD)
Head & Neck	0.1231 ± 0.0025	0.1963 ± 0.0102
Torso	0.2237 ± 0.0031	2.8508 ± 0.0349
Upper Arm (R / L)	0.149 ± 0.002 / 0.149 ± 0.001	0.0238 ± 0.0022 / 0.0236 ± 0.0002
Forearm (R / L)	0.108 ± 0.001 / 0.109 ± 0.003	0.0106 ± 0.0002 / 0.0104 ± 0.0007
Hand (R / L)	0.022 ± 0.001 / 0.021 ± 0.001	0.0022 ± 0.0001 / 0.0022 ± 0.0001
Thigh (R / L)	0.174 ± 0.001 / 0.173 ± 0.002	0.2225 ± 0.0139 / 0.2443 ± 0.0093
Shank (R / L)	0.147 ± 0.001 / 0.148 ± 0.001	0.0701 ± 0.0003 / 0.0664 ± 0.0014
Foot (R / L)	0.082 ± 0.002 / 0.087 ± 0.002	0.0060 ± 0.0002 / 0.0067 ± 0.0001

Synonymous with the Paralympian's equipment configuration, body DS (i.e., the delivery stick) was set to 1.96 m in length, 0.18 kg in mass, and the principal mass moment of inertia was calculated by modeling the delivery stick as a slender rod (i.e., $I_{zz} = \frac{1}{12}mL^2$). Body S (i.e., the curling stone) was given a mass of 19.96 kg and a height of 0.19 m; these quantities were taken from previous research (Maeno, 2014). Non-inertial reference frames were fixed to each rigid body segment.

2.2.2 Lower Kinematic Pairs

Referring back to Figure 2.4, joint HP represents the hip, joint SH is the shoulder, joint EL is the elbow, and joint WR is the wrist, all of which were modeled as revolute kinematic pairs. Joints HP, SH, and EL permit flexion-extension while joint WR allows for radial-ulnar deviation, assuming a neutral hand position. While these assumptions regarding the joint configurations appear to suffice for two-dimensional models, the shoulder joint abducts-adducts and the wrist pronates-supinates throughout the wheelchair curling delivery. Joint HP was set to 0.62 m above the inertial reference frame (i.e., simulating the height of the wheelchair seat). The revolute joints contained angular viscous damping, the quantities of which were taken from previous research (Table 2.4).

Table 2.4. Angular viscous damping coefficients about the hip, shoulder, elbow, and wrist (Lebiedowska, 2006; Rapoport et al, 2003).

Revolute Joint	Damping Coefficient (Nm·s/°)
Hip	41.3
Shoulder	80.3
Elbow	11.5
Wrist	4.0

A prismatic kinematic pair was used to model the contact between the curling stone and ice sheet. The stone can translate in the $+X$ direction and rotations about the vertical axis are omitted. Aerodynamic drag on the stone is presumably negligible, and thus was ignored. The contact model also included an opposing force vector representative of dry Coulomb friction (i.e., the product of the coefficient of dynamic friction and the normal force) wherein $\mu = 0.01$ (Maeno, 2014); this assumes the friction coefficient is constant throughout the delivery. Nyberg et al (2013) compared the translational stone velocities between i) assuming a constant coefficient of dynamic friction, and ii) including velocity dependency. The authors reported "similar" results between the two different methods (Nyberg et al, 2013). The multibody biomechanical model has 3 degrees of freedom and is mathematically represented by 4 ordinary differential equations and 1 algebraic equation (i.e., indicative of the model's kinematic constraints). With the establishment of a sufficient multibody biomechanical model, the kinematics and dynamics of the wheelchair curling delivery were subsequently investigated.

3 Multibody Kinematics and Dynamics

3.1 Experimental Kinematics

3.1.1 Inertial Measurement Units

The angular joint kinematics throughout the wheelchair curling delivery were experimentally measured using an inertial measurement unit (IMU) system (MVN Suit, Xsens Technologies, Netherlands). The system consists of 17 IMUs, which were attached to the Paralympian's head, torso, upper arms, forearms, hands, thighs, shanks, and feet. Each IMU contains a triaxial linear accelerometer, rate gyroscope, and magnetometer (Roetenberg, 2006). The linear accelerometers measure accelerations including the gravitational acceleration, the magnetometers measure the geomagnetic field, and the rate gyroscopes measure angular velocities. The IMU system is portable, wireless, and non-obstructive, making it appropriate for sport applications (e.g., wheelchair curling). The system utilises a 23-segment biomechanical model and proprietary algorithms to calculate the angular joint kinematics (Roetenberg, 2006).

Following a standard calibration of the IMU system (Roetenberg, 2006), the Paralympian performed 14 deliveries of the curling stone interspersed with 2 minutes of rest between deliveries. Recall that the objective in wheelchair curling is to deliver the stone in such a way that it rectilinearly translates along the ice sheet and lands within the house. Data were sampled at 120 Hz. High-frequency noise in the joint kinematic measurements was minimized during post-processing using smoothing splines (MATLAB, MathWorks, USA). Previous research has demonstrated the test-retest reliability (Cloete and Scheffer, 2010) and concurrent validity (Zhang et al, 2013) of the

IMU system in computing angular joint kinematics compared with optical motion capture.

3.1.2 Optical Motion Capture

Similar to the methods used by previous biomechanics research of Olympic curling (Yoo et al, 2012), movement of the curling stone was recorded with a digital camera (Nikon D3100, Nikon Corporation, Japan) that was positioned perpendicular to the Paralympian's plane of motion (Figure 3.1). The camera sampled at 29 frames per second. The translational stone kinematics (i.e., displacements and velocities) throughout the delivery were determined relative to an inertial reference frame using markerless feature tracking software (ProAnalyst, Xcitex Incorporation, USA). Scaling factors in the XY directions were computed via calibrating the dimensions of various objects within the digital recordings (i.e., the length of the delivery stick and height of the wheelchair seat) against known dimensions. Visual features of the curling stone (i.e., corners, textured areas, etc.) were extracted and tracked over multiple frames until the end of the delivery. The delivery is defined as the time duration between the initial displacement of the stone and its moment of release from the delivery stick. High-frequency noise in the stone kinematic measurements was minimized using smoothing splines (MATLAB, MathWorks, USA).

Figure 3.1. Field of view of the optical motion capture.

3.2 Kinematic Constraints

3.2.1 Optimization of Experimental Kinematics

The experimental kinematics were optimized to satisfy the kinematic constraints (i.e., specifically holonomic constraints) of the multibody biomechanical model. Holonomic constraints in human biomechanics include: i) anatomical, ii) actual, iii) mechanical, and iv) motor task constraints (Zatsiorsky, 1998; Ojeda et al, 2016). This research considers only anatomical and actual constraints. Anatomical constraints are those imposed by the structure of the human skeletal system (i.e., its geometry). Joints are typically constrained by adjacent body segments forming joint contacts and the joint ranges of motion. Actual constraints comprise physical obstacles to human movement (e.g., elements of the surrounding environment). In the multibody biomechanical model, these constraints include the wheelchair and the interaction between the curling stone

and ice sheet. To address the holonomic constraints of the multibody biomechanical model, a nonlinear constrained optimization algorithm was used to minimize the following multi-objective function at discrete time steps (i.e., j = 0…0.65 s and Δj resampled = 0.001 s)

$$\psi_j^{\dagger} = \text{Arg min}\left[\sum_{i=1}^{5} W_i \left(\frac{\psi_{ij}-\psi_{ij}^m}{\Delta\psi_i^m}\right)^2 + W_6\left(\frac{AE(\theta_{1j}\ldots\theta_{4j})}{L}\right)^2 + W_7\left(\frac{x_j - f(\theta_{1j}\ldots\theta_{4j})}{\Delta x^m}\right)^2\right] \quad (4)$$

subject to

$$\psi_{min}^m < \psi_j < \psi_{max}^m \quad (5)$$

where $\psi = [\theta_1\theta_2\theta_3\theta_4 x]^T$, ψ^m represents the experimentally measured ψ variables, $W_1\ldots W_7$ are weighting terms (i.e., W_1 = 15, W_2 = 0.1, W_3 = 0.95, W_4 = 1.5, W_5 = 200, W_6 = 100, and W_7 = 100) as determined via experimental trial and error, AE ($\theta_{1j}\ldots\theta_{4j}$) is the algebraic constraint equation from the multibody biomechanical model, and L (i.e., 0.43 m) is the vertical distance between the heights of the wheelchair seat and curling stone handle. $f(\theta_{1j}\ldots\theta_{4j})$ denotes the modeled displacement (x) of the curling stone (i.e., body S) in terms of the variables $\theta_1\ldots\theta_4$. Equation (5) specifies the minimum and maximum kinematic bounds on each ψ variable. The Paralympian's range of motion about joints HP (θ_1), SH (θ_2), EL (θ_3), and WR (θ_4) were experimentally measured using a digital goniometer. $\Delta\psi$ is the difference between ψ_{min}^m and ψ_{max}^m.

3.2.2 Optimized Kinematics

Figure 3.2 presents the angular displacements of joints HP, SH, EL, and WR throughout the delivery. Recall that the delivery is the time duration between the initial

displacement of the stone and its moment of release from the delivery stick. The quantities are displayed as arithmetic means over multiple deliveries with uncertainties expressed as ± 1 standard deviation. Joint SH had the largest range of motion (i.e., Δ 142.7 ± 3.1°) relative to joints HP (i.e., Δ 27.0 ± 2.9°), EL (i.e., Δ 96.7 ± 3.3°), and WR (i.e., Δ 22.8 ± 1.7°). The delivery was initiated through rotations about joint HP (i.e., flexion), followed sequentially by joints SH (i.e., flexion), EL (i.e., extension), and WR (i.e., ulnar-deviation); this kinematic sequencing resembles a follow-through delivery technique. The mean duration of the delivery was 0.65 seconds. In contrast, previous biomechanics research (Yoo et al, 2012) of Olympic curlers reported delivery times of 3.20 ± 0.14 seconds.

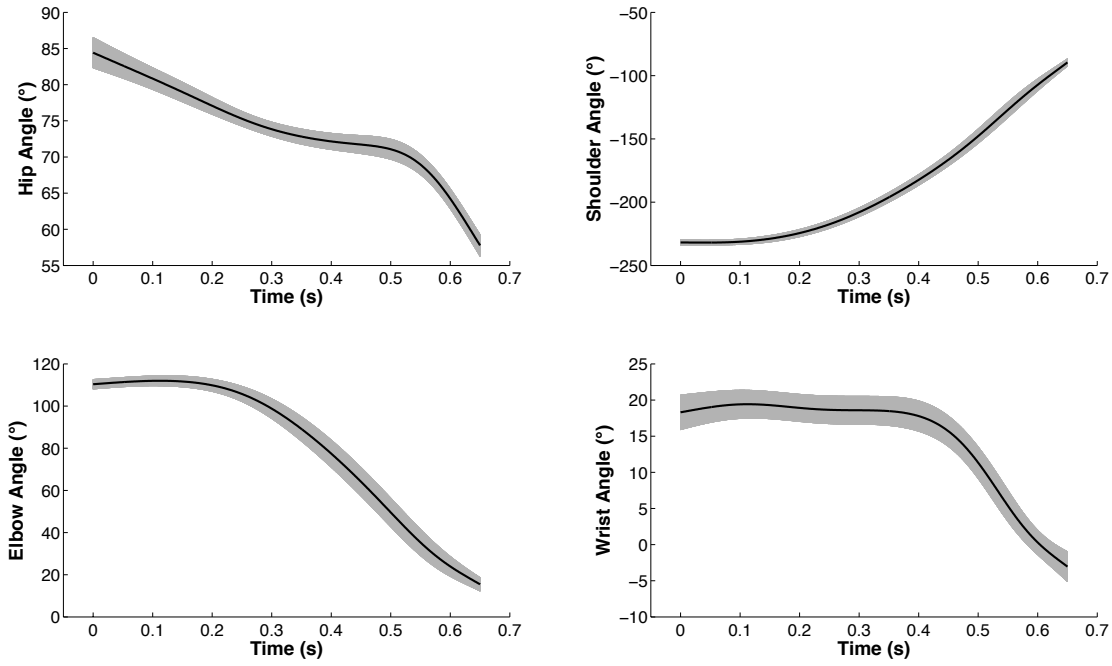

Figure 3.2. Relative angular displacements of the hip, shoulder, elbow, and wrist throughout the delivery.

Figure 3.3 presents the angular joint velocities as arithmetic means ± 1 standard deviation over multiple deliveries. The optimized velocities were computed via numerical differentiation of the optimized angular displacements. Joint HP had a maximum flexion velocity of -133.8 ± 10.2 °/s. Joint SH had a maximum flexion velocity of 427.2 ± 12.6 °/s and extension velocity of -4.1 ± 16.4 °/s. Joint EL had a maximum flexion velocity of 21.0 ± 13.3 °/s and extension velocity of -299.7 ± 16.7 °/s. Joint WR had a maximum radial-deviation velocity of 17.2 ± 9.6 °/s and ulnar-deviation velocity of -126.3 ± 12.1 °/s. Although the joint kinematics might be considered indicative of an "optimal" delivery technique (i.e., since the athlete is a Paralympic gold medalist), additional research is needed to ascertain the delivery kinematics of other Paralympic wheelchair curlers in order to derive statistically significant conclusions.

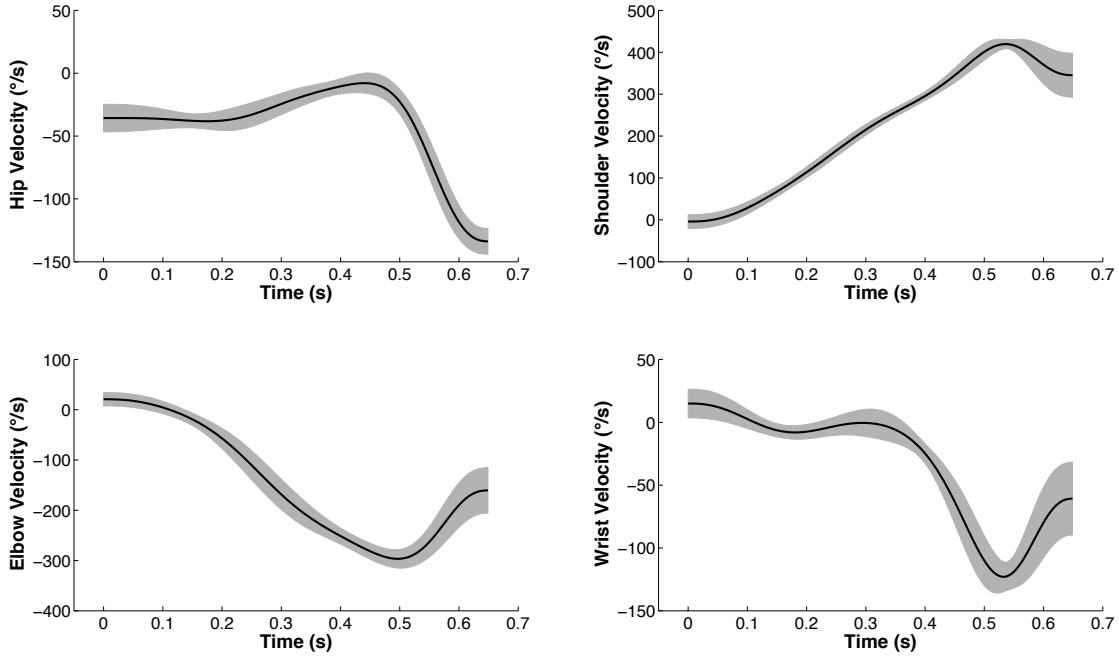

Figure 3.3. Angular velocities of the hip, shoulder, elbow, and wrist throughout the delivery.

Figure 3.4 presents the translational stone kinematics (i.e., displacements and velocities) as arithmetic means ± 1 standard deviation over multiple deliveries. The curling stone displaced a maximum of 0.80 ± 0.02 m throughout the delivery. In contrast, previous biomechanics research (Yoo et al, 2012) of Olympic curlers reported maximum displacements throughout the delivery of 5.04 ± 0.05 m. The translational stone velocity at the moment of release (i.e., 2.0 ± 0.1 m/s) correlated with that reported by recent mathematical models of curling mechanics (Maeno, 2014). There was minimal translational stone acceleration towards the end of the delivery; this is presumably brought about by the Paralympian to enhance precision. The Paralympian exhibited a high degree of inter-delivery consistency, as evidenced by the minor uncertainties in the stone kinematics.

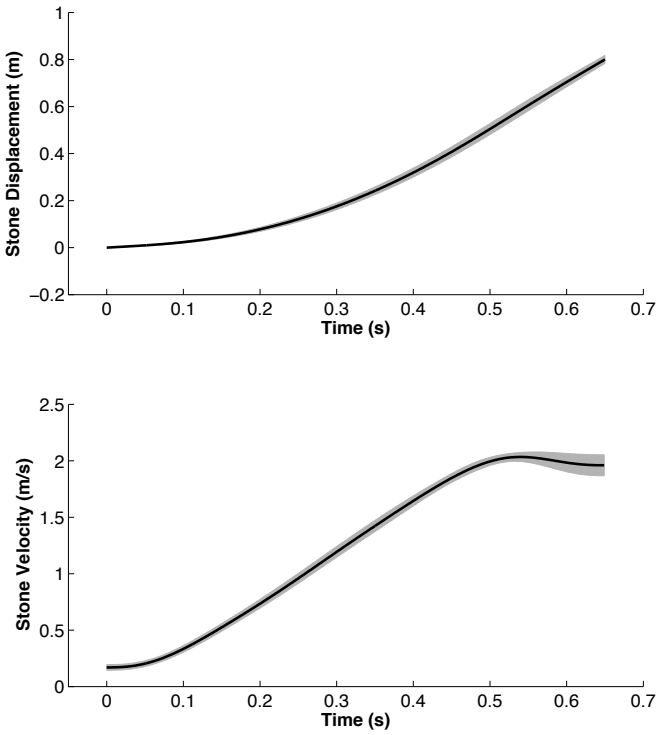

Figure 3.4. Translational stone kinematics (i.e., displacements and velocities) throughout the delivery.

3.3 Inverse Dynamics

3.3.1 Formulation

One of the main objectives of biomechanists is to evaluate the dynamics (i.e., forces and moments) associated with human movements. Experimentally measuring the forces of individual skeletal muscles (i.e., dynamometry) is invasive and therefore unpractical in sport environments (Roberston et al, 2014). With modern advancements in computer science, biomechanical modeling presents a viable method of approximating the dynamics of multibody movements (Roberston et al, 2014).

Inverse dynamics calculates the resultant forces and moments about individual joints by solving the Newton-Euler equations of motion given the kinematics and inertial parameters of adjacent body segments. MapleSim (i.e., the same software used to design the multibody biomechanical model) generates these dynamic equations in symbolic form using graph-theoretic algorithms, which significantly decreases the computation time compared with numerical methods. MapleSim was used to solve the Newton-Euler equations of motion for the resultant moments about joints HP, SH, and EL using the optimized kinematics. Joint WR was modeled as a passive joint (i.e., unactuated) in the interests of simulating the limited hand functionality of the Paralympic wheelchair curler. The passive joint moments were ignored. A process flow diagram of the inverse dynamics analysis is displayed in Figure 3.5. There has been only one previous investigation (Yoo et al, 2012) to compute the resultant joint moments of Olympic curlers throughout the delivery via inverse dynamics analysis. Nevertheless, since previous research focused on computations about the lower extremity joints, direct comparisons with the present work are not possible.

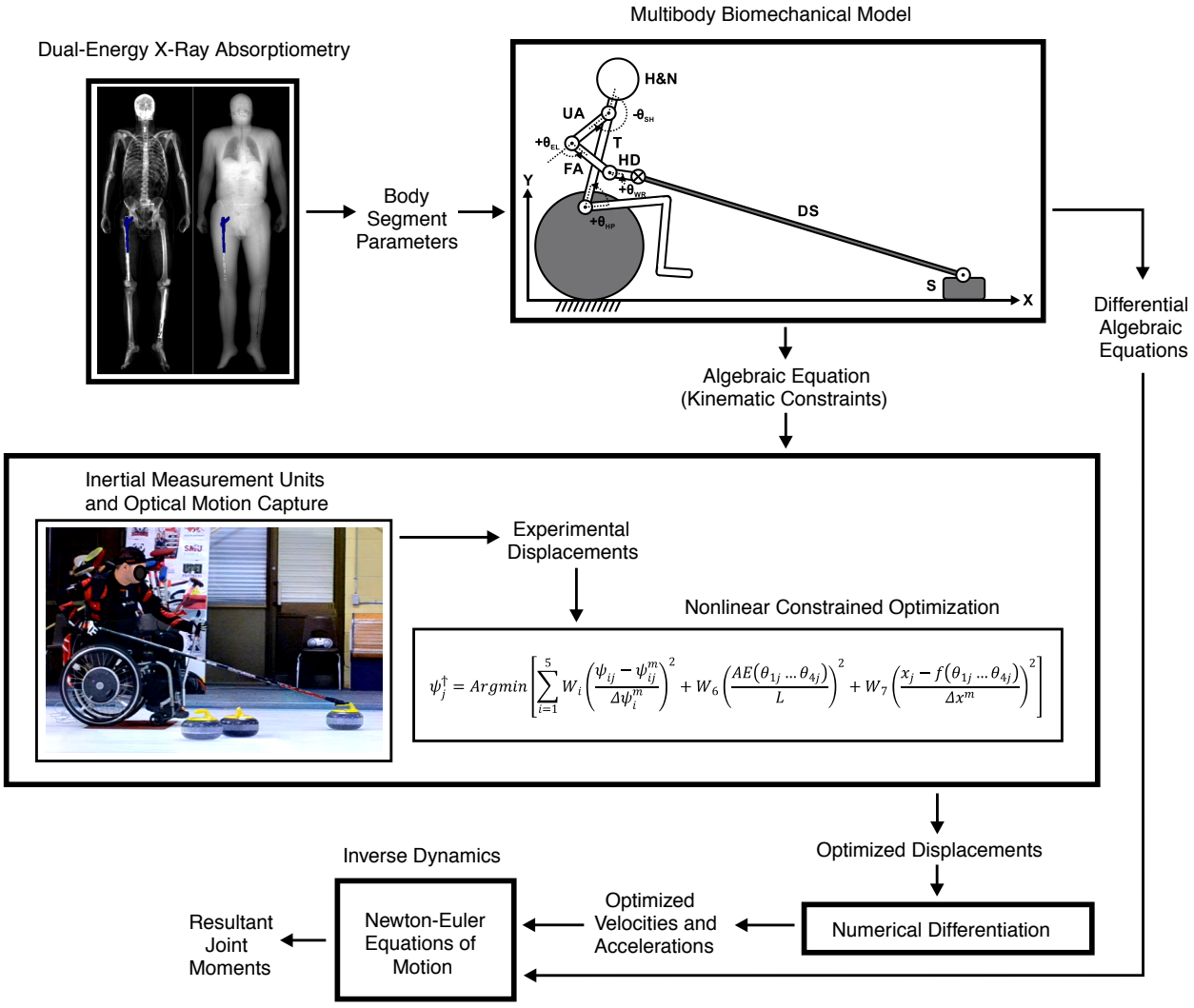

Figure 3.5. Flow diagram of the inverse dynamics.

3.3.2 Resultant Joint Moments

Figure 3.6 presents the resultant moments about joints HP, SH, and EL as computed via the inverse dynamics analysis. The quantities are displayed as arithmetic means over multiple deliveries with uncertainties expressed as ± 1 standard deviation. The largest moments were about joint HP (i.e., maximum of 203.2 ± 34.9 Nm), followed by joints SH (i.e., maximum of 54.6 ± 6.2 Nm) and EL (i.e., maximum of 12.6 ± 2.2 Nm). The

maximum resultant joint moments throughout the wheelchair curling delivery correlated with those previously reported during flexion-extension movements with able-bodied individuals (i.e., hip = 210 Nm, shoulder = 71 Nm, and elbow = 58 Nm)(Bober et al, 2002). Nevertheless, inverse dynamics is not predictive, and requires expensive and time-consuming experiments. Forward dynamics, by contrast, predicts the multibody kinematics by numerically integrating the Newton-Euler equations of motion given the forces and moments as inputs; these dynamic inputs are often elicited from mathematical models of neural excitations (Roberston et al, 2014). Accordingly, the following chapter investigates the neural motor control of the Paralympic wheelchair curler throughout the delivery.

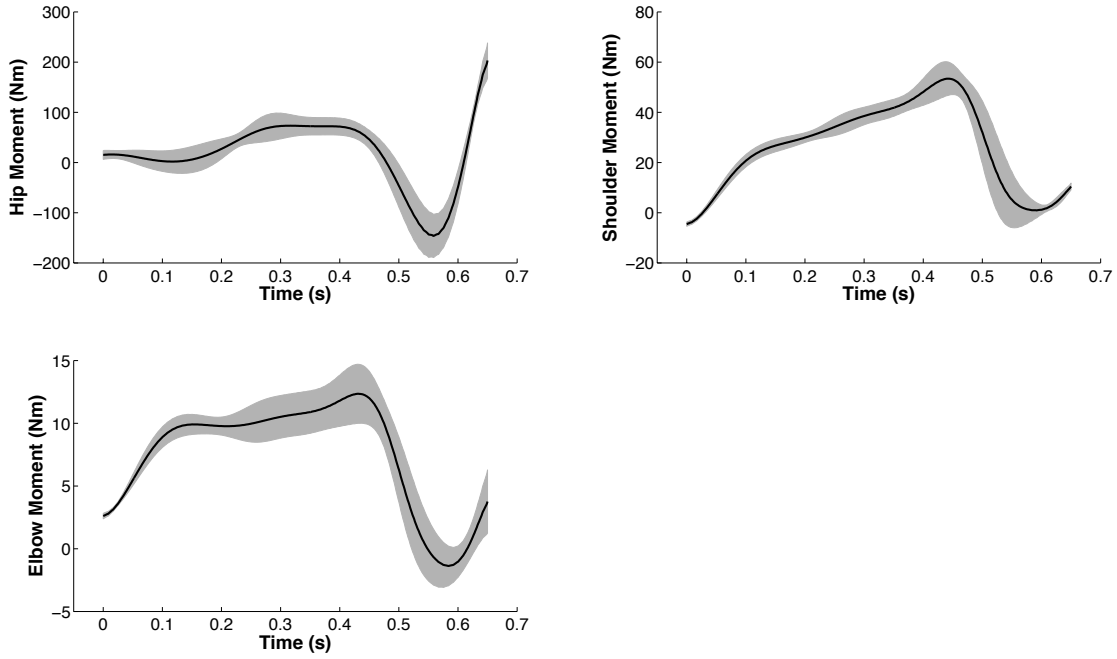

Figure 3.6. Resultant joint moments about the hip, shoulder, and elbow.

4 Neural Motor Control

4.1 Kinematic Redundancy

Neural motor control is the process through which the central nervous system (i.e., the brain and spinal cord) coordinates multibody movements. Human neural motor control is extremely complex insomuch as the skeletal system is kinematically redundant (i.e., there are more degrees of freedom than required to execute a particular movement). The human skeletal system has 244 degrees of freedom (Zatsiorsky, 1998). To position the hand (i.e., the end effector) in three-dimensional space, the central nervous system has to specify 244 variables, of which 238 are redundant (Zatsiorsky, 1998). The degrees of freedom in the joint space exceed those in the end effector space, thus leading to an indeterminant Jacobian. The Jacobian is a matrix of partial derivatives that mathematically relates the joint space and end effector space coordinates (Zatsiorsky, 1998).

Nikolai Bernstein originally identified the inherent kinematic redundancies of multibody human movements in the late 1960s (Bernstein, 1967). Nevertheless, biomechanists are still attempting to understand how the central nervous system controls the body's numerous degrees of freedom in light of the infinite number of potential solutions. The complexity of the musculoskeletal and central nervous systems has led biomechanists to develop computational models of the human body, which are innately simplified. Though the proposed multibody biomechanical model contains only 3 degrees of freedom, the system is kinematically redundant since only 2 degrees of freedom are required to specify the position of the curling stone.

4.2 Spinal Cord Injury

An emerging area of human movement science includes the neural motor control of individuals with spinal cord injuries. The spinal cord is a conduit through which motor and sensory information travels between the musculoskeletal and central nervous systems (Kirshblum et al, 2011). A spinal cord injury affects the conduction of motor and sensory signals across the sites of lesion, whereby key pathways necessary for signal transmission are disrupted (Prilutsky et al, 2011). Typical neural motor control pathologies following an incomplete spinal cord injury (i.e., similar to the Paralympic wheelchair curler) include: tonic physiological responses, spasticity, co-contraction, and inefficient timing of movements (Prilutsky et al, 2011). Information regarding how individuals with spinal cord injuries execute multibody movements can provide valuable insights into how the musculoskeletal and central nervous systems interact to control the body.

4.3 Optimization-Based Neural Motor Control

4.3.1 Forward Dynamic Optimization

Scientists have used optimization methods to computationally model how the central nervous system resolves kinematic redundancies (Sha and Thomas, 2015; Shoushtari, 2013). In particular, forward dynamic optimization involves solving the same problem that the central nervous system is confronted with (i.e., finding the neural excitations that drive multibody movements). In this manner, the neural motor control is mathematically modelled as an optimization problem, whereby a specified objective function is minimized (or maximized) subject to constraints (Porsa et al, 2016). The

advantage of this method lies in its predictive capability since it mimics the underlying neural motor control. The central nervous system uses an unknown algorithm, which unconsciously controls the human body (Porsa et al, 2016). One of the main challenges for biomechanists is choosing a representative objective function. In situations where the objective is not apparent, forward dynamic optimization can be used to evaluate different objectives to assess which function brings about multibody movements that resemble experimental measurements.

Forward dynamic optimization of the wheelchair curling delivery was computed in GPOPS-II (Patterson and Rao, 2012), which utilizes direct collocation. Direct collocation converts the differential algebraic equations into algebraic constraints by evaluating the system equations of motion at collocation points (i.e., nonlinear programming). Both the control and state variables are simultaneously approximated with unknown polynomial functions over the total time duration. Following an initial guess, the polynomials are iteratively updated through different mesh refinement methods (e.g., increasing the number of polynomials) until the objective function is minimized and the constraints are satisfied (Patterson and Rao, 2012). Accordingly, no numerical integration is required. Few investigations (Ackermann and van den Bogert, 2010; Miller and Hamill, 2015) have used direct collocation to predict multibody human movements. The trajectories of both the control variables (i.e., resultant joint moments) and state variables (i.e., kinematics) throughout the wheelchair curling delivery were predicted via minimizing each of the following objective functions

$$\left[\tau^{\dagger}_{(t)}, \psi^{\dagger}_{(t)}, \dot{\psi}^{\dagger}_{(t)}\right] = \text{Arg min}\left[\int_{t=0}^{t_F} \sum_{i=1}^{3} \tau^{2}_{i(t)}\, dt\right] \tag{6}$$

$$\left[\tau^{\dagger}_{(t)}, \psi^{\dagger}_{(t)}, \dot{\psi}^{\dagger}_{(t)}\right] = \text{Arg min}\left[\int_{t=0}^{t_F} \sum_{i=1}^{4} \dot{\theta}^{2}_{i(t)}\, dt\right] \tag{7}$$

$$\left[\tau_{(t)}^{\dagger}, \psi_{(t)}^{\dagger}, \dot{\psi}_{(t)}^{\dagger}\right] = \text{Arg min}\left[\int_{t=0}^{t_F} \sum_{i=1}^{4} \ddot{\theta}_{i(t)}^{2}\, dt\right] \tag{8}$$

$$\left[\tau_{(t)}^{\dagger}, \psi_{(t)}^{\dagger}, \dot{\psi}_{(t)}^{\dagger}\right] = \text{Arg min}\left[\int_{t=0}^{t_F} \sum_{i=1}^{3} \left(\tau_{i(t)}\dot{\theta}_{i(t)}\right)^{2} dt\right] \tag{9}$$

subject to

$$\psi_{min}^{m} < \psi_{(t)} < \psi_{max}^{m} \tag{10}$$

$$\psi_{(t=0)} = \psi_{tI} \tag{11}$$

$$\psi_{tF}^{lower} < \psi_{(t=tF)} < \psi_{tF}^{upper} \tag{12}$$

$$\begin{cases} \dot{\psi}_{(t)} = f\left(\psi_{(t)}, \tau_{(t)}, \lambda_{(t)}\right) \\ \quad g\left(\psi_{(t)}, \lambda_{(t)}\right) = 0 \end{cases} \tag{13}$$

where τ represents the controls, ψ represents the states, $\dot{\psi}$ are the time derivatives of ψ, t_F is the final time (i.e., 0.65 seconds), $\dot{\theta}$ are the angular joint velocities, $\ddot{\theta}$ are the angular joint accelerations, λ are the Lagrange Multipliers, and ψ_{tI} and ψ_{tF} are the state variables at the initial and final times, respectively. Recall that $\psi = [\theta_1\theta_2\theta_3\theta_4 x]^T$. Equation (13) denotes the system equations of motion, comprising 4 ordinary differential equations and 1 algebraic equation. The different optimization objective functions (i.e., equations 6-9) were taken from previous research (Hollerbach and Suh, 1987; Parnianpour et al, 1999; Zatsiorsky, 1998). The nonlinear programming was solved using IPOPT (Biegler and Zavala, 2008). A flow diagram of the forward dynamic optimization is presented in Figure 4.1. The predicted kinematics from the different optimization objective functions were compared with those experimentally measured throughout the wheelchair curling delivery.

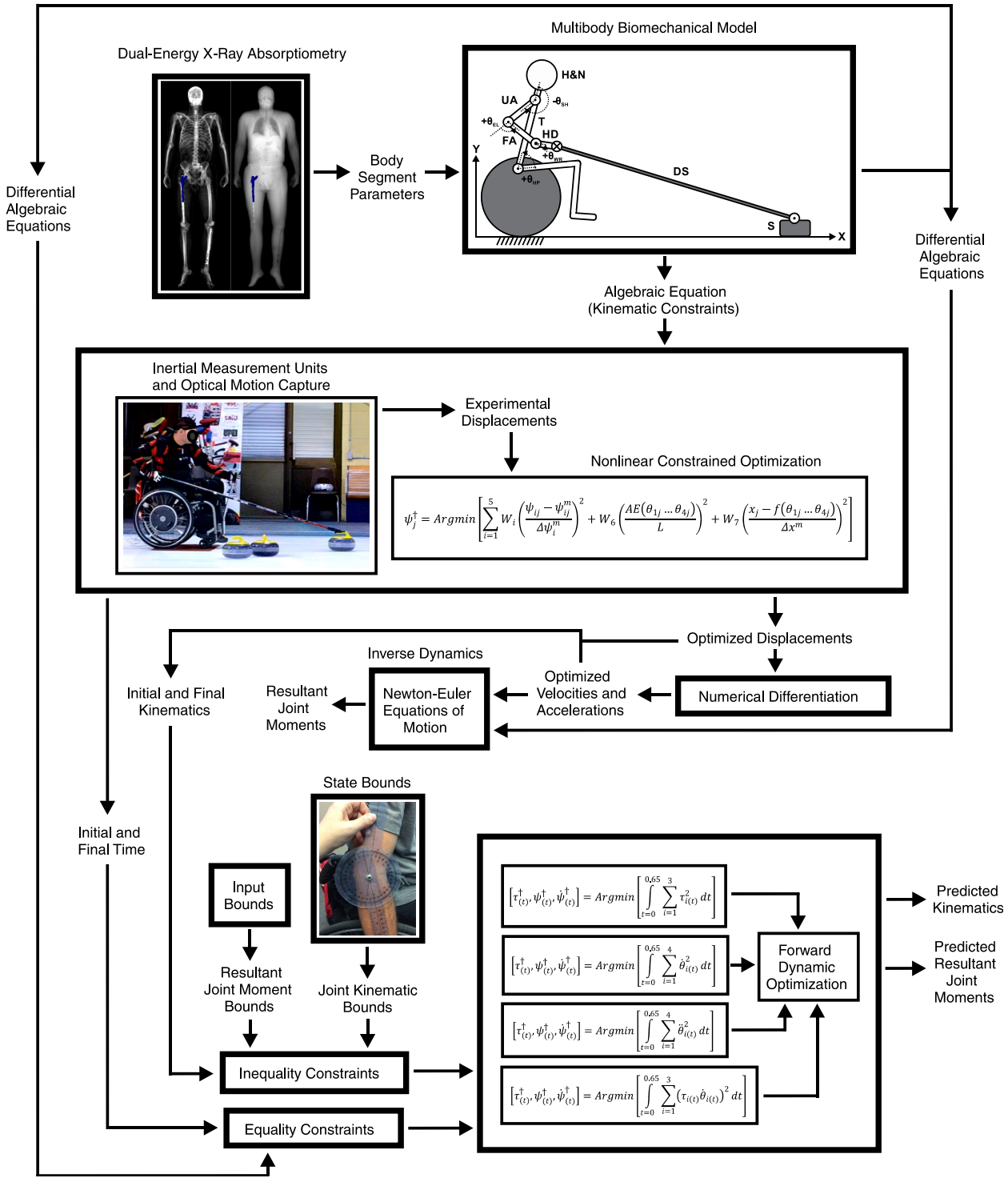

Figure 4.1. Flow diagram of the forward dynamic optimization.

4.3.2 Predictive Simulations

Figure 4.2 presents the angular displacements of joints HP, SH, EL, and WR throughout the delivery i) as experimentally measured using the inertial measurement unit system, and ii) as predicted via the different forward dynamic optimization objective functions. For joints HP, SH, and EL, all of the objective functions under consideration produced angular displacements that were in moderate qualitative agreement with the experimental kinematics. Minimizing angular joint accelerations was the only optimization objective function to accurately predict the angular displacements of joint WR. As expected, minimizing angular joint velocities produced straight-line angular displacement trajectories between the specified initial and final conditions.

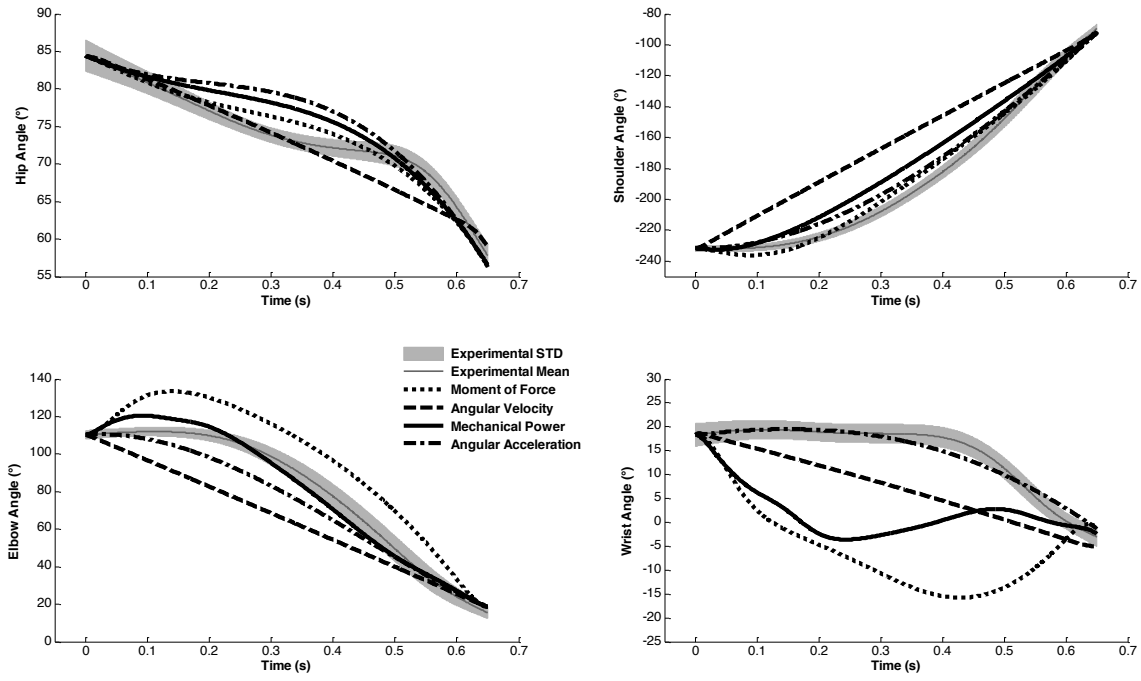

Figure 4.2. Experimental and predicted angular displacements of the hip, shoulder, elbow, and wrist throughout the delivery.

The root mean square error (RMSE) of each objective function was calculated in order to quantitatively assess the agreement between the experimental and predicted joint angles (Table 4.1). RMSEs are the square roots of the mean squared deviations between the experimental and predicted kinematics; a RMSE of zero denotes perfect agreement. Independent of the objective function being evaluated, joint HP had the lowest RMSEs, indicating that the forward dynamic optimization consistently and accurately predicted the angular displacements of the hip. Minimizing angular joint accelerations resulted in the lowest overall RMSEs relative to the other optimization objective functions.

Table 4.1. Root mean square errors of the predicted joint angles (°) relative to the experimental kinematics.

Joint	Moments	Angular Velocities	Mechanical Power	Angular Accelerations
Hip	2.0 ± 0.6	2.4 ± 0.6	2.8 ± 0.7	3.6 ± 0.7
Shoulder	5.8 ± 1.6	28.3 ± 3.0	12.6 ± 2.9	7.6 ± 2.4
Elbow	17.4 ± 3.9	19.9 ± 3.4	6.6 ± 2.0	9.9 ± 3.3
Wrist	23.0 ± 1.6	8.6 ± 1.6	14.9 ± 1.6	2.4 ± 0.8

Figure 4.3 presents the experimental and predicted angular velocities of joints HP, SH, EL, and WR throughout the delivery. None of the optimization objective functions predicted angular velocities that had sufficient qualitative agreement with the experimental kinematics. Nonetheless, minimizing angular joint accelerations resulted in the smoothest angular velocity trajectories. Minimizing angular joint velocities produced straight-line horizontal kinematic trajectories between the specified initial and final conditions.

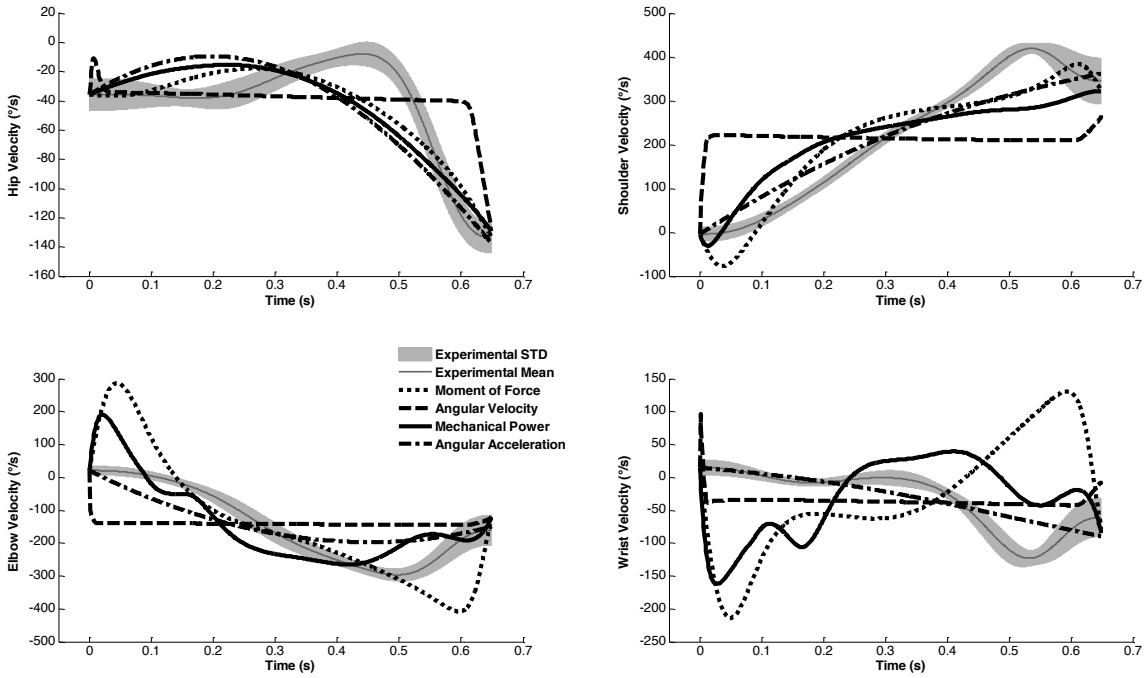

Figure 4.3. Experimental and predicted angular velocities of the hip, shoulder, elbow, and wrist throughout the delivery.

The RMSEs of the predicted angular joint velocities are displayed in Table 4.2. The quantities are significantly larger than those previously reported for the predicted angular displacements. This indicates that, independent of the objective function being evaluated, the forward dynamic optimization was less accurate in predicting the angular joint velocities compared with the angular displacements. Minimizing angular joint accelerations resulted in the lowest overall RMSEs relative to the other objective functions. Analogous with Olympic curling (Yoo et al, 2012), wheelchair curling is a target-directed sport wherein both the accuracy and consistency of the delivery are paramount to success. Accordingly, minimizing angular joint accelerations appears to be a logical solution to the proposed optimization problem (i.e., in order to enhance the Paralympian's precision towards the moment of release).

Table 4.2. Root mean square errors of the predicted angular joint velocities (°/s) relative to the experimental kinematics.

Joint	Moments	Angular Velocities	Mechanical Power	Angular Accelerations
Hip	19.2 ± 2.8	28.7 ± 4.8	23.0 ± 3.0	26.5 ± 3.4
Shoulder	57.7 ± 4.6	146.5 ± 9.3	77.8 ± 7.7	50.5 ± 5.6
Elbow	108.6 ± 11.6	111.6 ± 8.8	69.8 ± 10.1	64.2 ± 9.9
Wrist	130.0 ± 6.0	44.40 ± 5.7	81.6 ± 4.5	26.1 ± 6.0

Figure 4.4 presents the translational stone kinematics (i.e., displacements and velocities) throughout the delivery. Apart from minimizing the angular joint velocities, all of the optimization objective functions predicted translational stone displacements that were in good qualitative agreement with the experimental kinematics. These findings were quantitatively exemplified through the RMSEs displayed in Table 4.3. Recall that the measured translational stone velocity at the moment of release was 2.0 ± 0.1 m/s. Though the initial and final conditions of the states (i.e., the kinematics) were specified in accordance with the experimental measurements, the final conditions were allocated a range of quantities, which characterized the Paralympian's inter-delivery inconsistencies. Therefore, the predicted translational stone velocities at the moment of release slightly differed from the experimental kinematics.

Table 4.3. Root mean square errors of the predicted translational stone kinematics relative to the experimental measurements.

Stone Kinematics	Moments	Angular Velocities	Mechanical Power	Angular Accelerations
Displacement (m)	0.019 ± 0.008	0.148 ± 0.012	0.054 ± 0.012	0.018 ± 0.008
Velocity (m/s)	0.154 ± 0.024	0.809 ± 0.022	0.319 ± 0.023	0.109 ± 0.026

Minimizing angular joint accelerations resulted in the shortest optimization computation time (i.e., 61 CPU seconds), followed sequentially by mechanical power (i.e., 269 CPU seconds), joint moments (i.e., 361 CPU seconds), and angular velocities (i.e., 1283 CPU seconds). It is important to emphasize that, while minimizing angular joint accelerations produced the most accurate kinematic trajectories (i.e., the lowest overall RMSEs) and the shortest optimization computation time, none of the objective functions under consideration perfectly simulated the experimental kinematics (and thus neural motor control) of the Paralympic wheelchair curler.

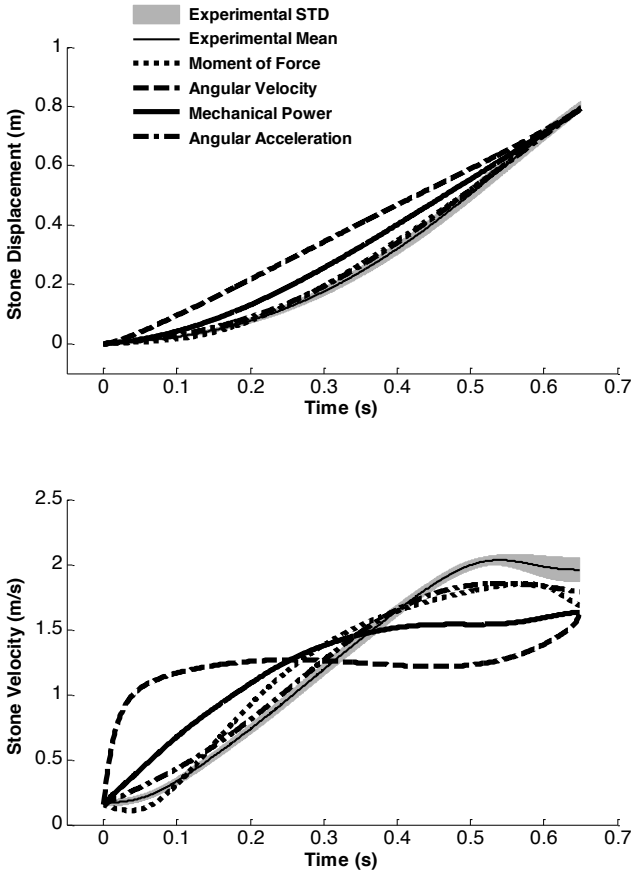

Figure 4.4. Experimental and predicted translational stone kinematics (i.e., displacements and velocities) throughout the delivery.

5 Conclusions and Future Research

5.1 Dual-Energy X-Ray Absorptiometry

The body segment parameters of the Paralympic wheelchair curler were experimentally measured using DXA imaging. Though previous research has established the validity of using DXA imaging to quantify the body segment parameters of able-bodied individuals (Durkin et al, 2002; Durkin and Dowling, 2003), particular consideration is needed for Paralympic athletes due to the presence of metallic implants. Whenever the DXA beam is radiated against a metallic implant (e.g., stainless steel or titanium), the photons are attenuated through Compton scattering and photoelectric absorption, and insufficient amounts of data transmit through to the DXA receiver. Consequently, the mass of that area cannot be computed. The effects of these omissions were made evident when analyzing the masses of the left and right thigh segments of the Paralympic athlete considering the femoral intramedullary implant in his right femur, as previously displayed in Figure 2.3. The asymmetrical differences in mass between the two thigh segments were approximately 20.1 %. Future research should consider developing model-based and/or experimental techniques to compensate for the DXA instrumentation omitting the masses of the pixels coinciding with metallic implants.

5.2 Musculoskeletal Modelling

The multibody biomechanical model evaluated the resultant moments about the lower back and upper extremity joints throughout the wheelchair curling delivery. Resultant joint moments are mathematical summations of the dynamics from all neighbouring biological elements (e.g., skeletal muscles, tendons, ligaments, and bursae) (Robertson

et al, 2014). Consequently, the forces and moments from individual skeletal muscles cannot be determined. This limits the applicability of the multibody biomechanical model considering that, for instance, the upper extremity contains antagonistic pairs (Robertson et al, 2014). The positive resultant moment about the elbow joint, as previously illustrated in Figure 3.6, could be attributed to either activations of the agonist muscles (e.g., biceps brachii) or deactivations of the antagonist muscles (e.g., triceps brachii). Future research should extend the multibody biomechanical model to a musculoskeletal model in order to evaluate the activations and dynamics of individual skeletal muscles throughout the delivery. These models could provide novel insights into the documented incidences of musculoskeletal injuries amongst Paralympic wheelchair curlers (Webborn et al, 2012).

5.3 Optimal Equipment Design

The neural motor control of the Paralympic athlete was modelled using forward dynamic optimization. Forward dynamic optimization also possesses the distinct capability of i) predicting the effects of model parameters on performance outcomes (i.e., sensitivity analyses) and ii) optimizing equipment designs to improve performance and/or minimize the risk of musculoskeletal injuries (Xiang et al, 2010). This approach allows for predictive "what if" simulations, such as "what if the mechanical parameters of the delivery stick (e.g., mass or length) were altered" and "what if the height of the wheelchair seat was changed". At present, the configurations of both the delivery stick and wheelchair are generally selected based on the athlete's subjective preferences rather than quantitative analysis. Predictive simulations could help shed light on these unanswered and potentially important questions.

Forward dynamic optimization can be used to evaluate optimal equipment designs *in silico*, thereby minimizing the search space in experimental trial and errors (Xiang et al, 2010). Suppose the research objective is to maximize translational stone velocity at the moment of release via optimizing the length of the delivery stick. Experimentally, a variety of different stick lengths would have to be investigated, as well as numerous trials per length in order to account for intra-athlete inconsistencies (Laschowski et al, 2015). Repetitive trials could bring about neuromuscular fatigue, thus affecting the validity of the experimental findings. Forward dynamic optimization, by contrast, does not require expensive and time-consuming experiments in order to attain a solution. Future research should consider utilizing the proposed multibody biomechanical model (i.e., comprising subject-specific body segments parameters, multibody kinematics and dynamics, and neutral motor control) to predict the effects of model parameters on Paralympic sport performance and/or optimize equipment designs prior to prototyping.

References

Ackermann M and van den Bogert AJ. (2010). Optimality Principles for Model-Based Prediction of Human Gait. Journal of Biomechanics. 43: 1055-1060.

Andrews JG and Mish SP. (1996). Methods for Investigating the Sensitivity of Joint Resultants to Body Segment Parameter Variations. Journal of Biomechanics. 29: 651-654.

Bernstein N. (1967). The Co-Ordination and Regulation of Movements. Pergamon Press: USA.

Biegler LT and Zavala VM. (2008). Large-scale Nonlinear Programming Using IPOPT: An Integrating Framework for Enterprise-Wide Optimization. Computers and Chemical Engineering. 33: 575-582.

Bober T, Kulig K, Burnfield JM, and Pietraszewski B. (2002). Predictive Torque Equations for Joints of the Extremities. Acta of Bioengineering and Biomechanics. 4: 49-61.

Bulbulian R, Johnson RE, Gruber JJ, and Darabos B. (1987). Body Composition in Paraplegic Male Athletes. Medicine and Science in Sports and Exercise. 19: 195-201.

Clauser CE, McConville JT, and Young JW. (1969). Weight, Volume and Center of Mass of Segments of the Human Body. Aerospace Medical Research Laboratory Technical Report 60-70. Wright Patterson Air Force Base: USA.

Cloete T and Scheffer C. (2010). Repeatability of an Off-The-Shelf, Full Body Inertial Motion Capture System During Clinical Gait Analysis. Proceedings of the IEEE 32nd

Annual International Conference of the Engineering in Medicine and Biology Society. 5125-5128.

Dempster WT. (1955). Space Requirements of the Seated Operator: Geometrical, Kinematic, and Mechanical Aspects of the Body with Special Reference to the Limbs. Wright Air Development Center Technical Report 55-159. Wright-Patterson Air Force Base: USA.

Durkin JL, Dowling JJ, and Andrews DM. (2002). The Measurement of Body Segment Inertial Parameters Using Dual Energy X-Ray Absorptiometry. Journal of Biomechanics. 35: 1575-1580.

Durkin JL and Dowling JJ. (2003). Analysis of Body Segment Parameter Differences Between Four Human Populations and The Estimation Errors of Four Popular Mathematical Models. Journal of Biomechanical Engineering. 125: 515-522.

GE Healthcare Lunar. (2013). enCORE-based X-ray Bone Densitometer: User Manual. Wisconsin: USA.

Goktepe AS, Yilmaz B, Alaca R, Yazicioglu K, Mohur H, and Gunduz S. (2004). Bone Density Loss After Spinal Cord Injury: Elite Paraplegic Basketball Players vs. Paraplegic Sedentary Persons. American Journal of Physical Medicine and Rehabilitation. 83: 279-283.

Hobara H, Potthast W, Muller R, Kobayashi Y, Heldoorn TA, and Mochimaru M. (2016). Normative Spatiotemporal Parameters During 100-m Sprint in Amputee Sprinters Using Running-Specific Prostheses. Journal of Applied Biomechanics. 32: 93-96.

Hollerbach JM and Suh KC. (1987). Redundancy Resolution of Manipulators through Torque Optimization. IEEE Journal of Robotics and Automation. RA-3: 308-316.

Inukai Y, Takahashi K, Wang DH, and Kira S. (2006). Assessment of Total and Segmental Body Composition in Spinal Cord-Injured Athletes in Okayama Prefecture of Japan. Acta Medica Okayama. 60: 99-106.

Keil M, Totosy de Zepetnek JO, Brooke-Wavell K, and Goosey- Tolfrey VL. (2016). Measurement Precision of Body Composition Variables in Elite Wheelchair Athletes, using Dual-Energy X-Ray Absorptiometry. European Journal of Sport Science. 16: 65-71.

Keogh JWL. (2011). Paralympic Sport: An Emerging Area For Research and Consultancy in Sports Biomechanics. Sports Biomechanics. 10: 234-253.

Kingma I, Toussaint HM, De Looze MP, and Van Dieen JH. (1996). Segment Inertial Parameter Evaluation in Two Anthropometric Models by Application of a Dynamic Linked Segment Model. Journal of Biomechanics. 29: 693-704.

Kirshblum et al. (2011). International Standards for Neurological Classification of Spinal Cord Injury (Revised 2011). The Journal of Spinal Cord Medicine. 34: 535-546.

Kocina P. (1997). Body Composition of Spinal Cord Injured Adults. Sports Medicine. 23: 48-60.

Lee MK, Le NS, Fang AC, and Koh MTH. (2009). Measurement of Body Segment Parameters using Dual Energy X-Ray Absorptiometry and Three-Dimensional Geometry: An Application in Gait Analysis. Journal of Biomechanics. 42: 217-222.

Laschowski B and McPhee J. (2016a). Quantifying Body Segment Parameters Using Dual-Energy X-Ray Absorptiometry: A Paralympic Wheelchair Curler Case Report. Procedia Engineering. 147C: 163-167.

Laschowski B and McPhee J. (2016b). Body Segment Parameters of Paralympic Athletes From Dual-Energy X-Ray Absorptiometry. Sports Engineering. DOI:10.1007/s12283-016-0200-3.

Laschowski B, Mehrabi N, and McPhee J. (2016). Optimal Control of Paralympic Wheelchair Curling. Proceedings of the 19th Biennial Meeting of the Canadian Society for Biomechanics. Hamilton: Canada.

Laschowski B, Nolte V, Adamovsky M, and Alexander R. (2015). The Effects of Oar-Shaft Stiffness and Length on Rowing Biomechanics. Journal of Sports Engineering and Technology. 229: 239-247.

Lebiedowska MK. (2006). Dynamic Properties of Human Limb Segments. In: Karwowski W, ed. International Encyclopaedia of Ergonomics and Human Factors. 2nd ed. CRC Press: USA. 315-319.

Maeno N. (2014). Dynamics and Curl Ratio of a Curling Stone. Sports Engineering. 17: 33-41.

Mason BS, van der Woude LHV, and Goosey-Tolfrey VL. (2013). The Ergonomics of Wheelchair Configuration for Optimal Performance in the Wheelchair Court Sports. Sports Medicine. 43: 23-38.

Miller RH and Hamill J. (2015). Optimal Footfall Patterns for Cost Minimization in Running. Journal of Biomechanics. 48: 2858-2864.

Mojtahedi MC, Valentine RJ, and Evans EM. (2009). Body Composition Assessment in Athletes with Spinal Cord Injury: Comparison of Field Methods with Dual-Energy X-Ray Absorptiometry. Spinal Cord. 47: 698-704.

Morrow MM, Rankin JW, Neptune RR, and Kaufman KR. (2014). A Comparison of Static and Dynamic Optimization Muscle Force Predictions During Wheelchair Propulsion. Journal of Biomechanics. 47: 3459-3465.

Nyberg H, Hogmark S, and Jacobson S. (2013). Calculated Trajectories of Curling Stones Sliding Under Asymmetrical Friction: Validation of Published Models. Tribology Letter. 50: 379-385.

Ojeda J, Martinez-Reina J, and Mayo J. (2016). The Effect of Kinematic Constraints in the Inverse Dynamics Problem in Biomechanics. Multibody System Dynamics. 37: 291-309.

Parnianpour A, Wang JL, Shirazi-Adl A, Khayatian B, and Lafferriere G. (1999). Computation Method for Simulation of Trunk Motion: Towards a Theoretical Based Quantitative Assessment of Trunk Performance. Biomedical Engineering: Applications, Basis and Communications. 11: 27-39.

Patterson MA and Rao AV. (2012). GPOPS II: A MATLAB Software for Solving Multiple-Phase Optimal Control Problems Using hp-Adaptive Gaussian Quadrature Collocation Methods and Sparse Nonlinear Programming. ACM Transactions on Mathematical Software. 41: 1-37.

Porsa S, Lin YC, and Pandy MG. (2016). Direct Methods for Predicting Movement Biomechanics Based Upon Optimal Control Theory with Implementation in OpenSim. Annals of Biomedical Engineering. 44: 2542-2557.

Prilutsky et al. (2011). Motor Control and Motor Redundancy in the Upper Extremity: Implications for Neurorehabilitation. Topics in Spinal Cord Injury Rehabilitation. 17: 7-15.

Rankin JW, Kwarciak AM, Richter WM, and Neptune RR. (2012). The Influence of Wheelchair Propulsion Technique on Upper Extremity Muscle Demand: A Simulation Study. Clinical Biomechanics. 27: 879-886.

Rao G, Amarantini D, Berton E, and Favier D. (2006). Influence of Body Segments' Parameters Estimation Models on Inverse Dynamics Solutions During Gait. Journal of Biomechanics. 39: 1531-1536.

Rapoport S, Mizrahi J, Kimmel E, Verbitsky O, and Isakov E. (2003). Constant and Variable Stiffness and Damping of the Leg Joints in Human Hopping. Journal of Biomechanical Engineering. 125: 507-514.

Roberston DGE, Caldwell GE, Hamill J, Kamen G, and Whittlesey SN. (2014). Research Methods in Biomechanics. 2nd ed. Human Kinetics: USA.

Roetenberg D. (2006). Inertial and Magnetic Sensing of Human Motion. [PhD Dissertation]. University of Twente: The Netherlands.

Sha D, Thomas JS. (2015). An Optimisation-Based Model For Full-Body Upright Reaching Movements. Computer Methods in Biomechanics and Biomedical Engineering Journal 18: 847-860.

Shoushtari AL. (2013). What Strategy Central Nervous System Uses to Perform a Movement Balanced? Biomechatronical Simulation of Human Lifting. Applied Bionics and Biomechanics. 10: 113-124.

Slowik SJ and Neptune RR. (2013). A Theoretical Analysis of the Influence of Wheelchair Seat Position on Upper Extremity Demand. Clinical Biomechanics. 28: 378-385.

Sutton L, Wallace J, Goosey-Tolfrey V, Scott M, and Reilly T. (2009). Body Composition of Female Wheelchair Athletes. International Journal of Sports Medicine. 30: 259-265.

Usma-Alvarez CC, Fuss FK, and Subic A. (2014). User-Centered Design Customization of Rugby Wheelchairs Based on the Taguchi Method. Journal of Mechanical Design. 136: 1-13.

Vanlandewijck YC and Thompson WR. (2011). Handbook of Sports Medicine and Science: The Paralympic Athlete. Wiley-Blackwell: UK.

Webborn N, Willick S, and Emery CA. (2012). The Injury Experience at the 2010 Winter Paralympic Games. Clinical Journal of Sports Medicine. 22: 3-9.

Weyand PG, Bundle MW, McGowan CP, Grabowski A, Brown MB, Kram R, and Herr H. (2009). The Fastest Runner on Artificial Legs: Different Limbs, Similar Function? Journal of Applied Physiology. 107: 903-911.

World Curling Federation. (2014). The Rules of Curling and Rules of Competition. Report from the World Curling Federation: Scotland.

Xiang Y, Arora JS, and Abdel-Malek K. (2010). Physics-Based Modeling and Simulation of Human Walking: A Review of Optimization-Based and Other Approaches. Structural and Multidisciplinary Optimization. 42: 1-23.

Yoo KS, Kim HK, and Park JH. (2012). A Biomechanical Assessment of the Sliding Motion of Curling Delivery in Elite and Subelite Curlers. Journal of Applied Biomechanics. 28: 694-700.

Zatsiorsky VM. (1998). Kinematics of Human Motion. Human Kinetics: USA.

Zhang JT, Novak AC, Brouwer B, and Li Q. (2013). Concurrent Validation of Xsens MVN Measurement of Lower Limb Joint Angular Kinematics. Physiological Measurement. 34: 63-69.

Appendices

Appendix 1. Ethics Approval for Dual-Energy X-Ray Absorptiometry

CSIO Research Ethics Board

MEMORANDUM

DATE: July 20th, 2015

TO: Dr. John McPhee, Principle Investigator

Brock Laschowski, Co-Investigator

FROM: Dr. Heather Sprenger, Lead of Physiology, Research & Innovation

REB #: 2015-03

Title: **Body Segment Parameters Using Dual-Energy X-Ray Absorptiometry: A Paralympic Case Study**

Thank-you for submitting your proposal amendments to the CSIO Research Ethics Board (REB).

The Canadian Sport Institute REB has reviewed the methodologies of your study and has granted your project approval. Your project has been assigned an REB #2015-03.

If this project changes in anyway, **you have the explicit responsibility to notify the Lead of Research & Innovation at that time in writing.**

Research records must be retained for a minimum of 3 years after completion of the research; if the study involves medical treatment, it is recommended that the results are retained for 5 years.

You are responsible for notifying all parties about the approval of this project, including your co-investigators, PSO/NSO coaches, and management. Please be advised that you will need to submit a progress report every 6 months until the study is completed and a final report outlining the key findings of the study.

Good luck with your research pursuits,

Dr. Heather Sprenger, PhD, Lead, Physiology & Research

Appendix 1.1. Ethics approval from the Canadian Sport Institute Ontario Research Ethics Board.

Appendix 2. Ethics Approval for On-Ice Kinematic Experiments

UNIVERSITY OF WATERLOO

OFFICE OF RESEARCH ETHICS

Notification of Ethics Clearance of Application to Conduct Research with Human Participants

Principal/Co-Investigator: Dr. John McPhee	**Department:** Systems Design Engineering
Principal/Co-Investigator: Dr. Naser Mehrabi	**Department:** Systems Design Engineering
Faculty Supervisor: Dr. John McPhee	**Department:** Systems Design Engineering
Student Investigator: Brock Laschowski	**Department:** Mechanical Engineering
Student Investigator: Reza Sharif Razavian	**Department:** Systems Design Engineering

ORE File #: 20584

Project Title: Biomechanics of Wheelchair Curling

This certificate provides confirmation the above project has been reviewed in accordance with the University of Waterloo's Guidelines for Research with Human Participants and the Tri-Council Policy Statement: Ethical Conduct for Research Involving Humans. This project has received ethics clearance through a University of Waterloo Research Ethics Committee.

***Note 1**: This ethics clearance is valid for one year from the date shown on the certificate and is renewable annually. Renewal is through completion and ethics clearance of the Annual Progress Report for Continuing Research (ORE Form 105).*

***Note 2**: This project must be conducted according to the application description and revised materials for which ethics clearance has been granted. All subsequent modifications to the project also must receive prior ethics clearance (i.e., Request for Ethics Clearance of a Modification, ORE Form 104) through a University of Waterloo Research Ethics Committee and must not begin until notification has been received by the investigators.*

***Note 3**: Researchers must submit a Progress Report on Continuing Human Research Projects (ORE Form 105) annually for all ongoing research projects or on the completion of the project. The Office of Research Ethics sends the ORE Form 105 for a project to the Principal Investigator or Faculty Supervisor for completion. If ethics clearance of an ongoing project is not renewed and consequently expires, the Office of Research Ethics may be obliged to notify Research Finance for their action in accordance with university and funding agency regulations.*

***Note 4**: Any unanticipated event involving a participant that adversely affected the participant(s) must be reported immediately (i.e., within 1 business day of becoming aware of the event) to the ORE using ORE Form 106. Any unanticipated or unintentional changes which may impact the research protocol must be reported within seven days of the deviation to the ORE using ORE form 107.*

SG

Maureen Nummelin, PhD
Chief Ethics Officer

4/2/2015
Date

OR
Julie Joza, MPH

Appendix 2.1. Ethics approval from the University of Waterloo Office of Research Ethics.

Appendix 3. Dual-Energy X-Ray Absorptiometry Scans of Team Canada

The following research experimentally measured the body segment parameters (i.e., mass, length, position vector of the center of mass, and principal mass moment of inertia about the center of mass) of Team Canada Paralympic athletes using DXA imaging (Laschowski and McPhee, 2016b). The sample included the Canadian Paralympic Wheelchair Curling Team ($n = 6$). Canada has won every gold medal in wheelchair curling at the Paralympic Games since its inauguration in 2006. A description of each Paralympian is provided in Appendix 3.1; the sample encompassed a variety of physical disabilities. For athletes with spinal cord injuries (SCI), motor impairments were characterized by the ASIA Impairment Scale. The Paralympic athlete to whom this thesis is based upon is labeled as Paralympian A5. Total body DXA scans of each Paralympic athlete are displayed in Appendix 3.2.

Appendix 3.1. The physical disability of each Paralympic athlete.

Code	Physical Disability	Metallic Implant	ASIA
A1	Unilateral Transfemoral Amputation	N/A	N/A
A2	Incomplete SCI Between 12^{th} Thoracic and 1^{st} Lumbosacral Vertebrae	Stainless Steel Harrington Implants	C
A3	Bilateral Total Knee Replacements	Type 2 Titanium Implants	N/A
A4	Complete SCI Between 11^{th} and 12^{th} Thoracic Vertebrae	N/A	A
A5	Incomplete SCI Between 5^{th} and 6^{th} Cervical Vertebrae	Titanium Intramedullary Implant	C
A6	Complete SCI Between 5^{th} and 6^{th} Thoracic Vertebrae	Stainless Steel Harrington Implants and Intrathecal Baclofen Pump	A

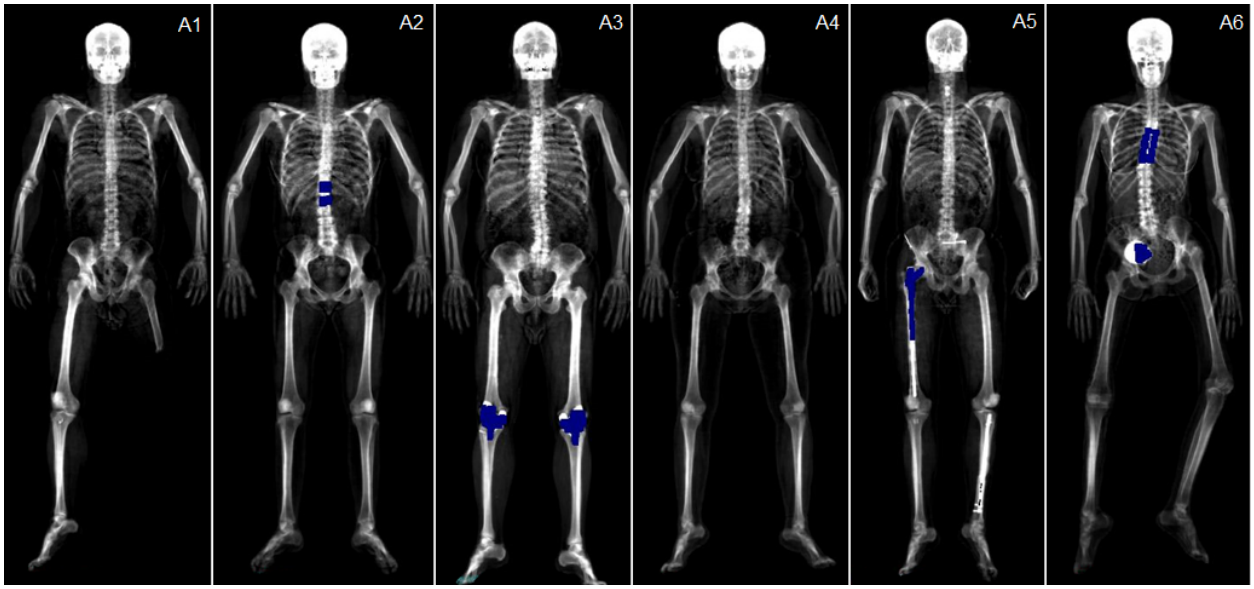

Appendix 3.2. Total body DXA scans of each Paralympic athlete.

The length of each body segment for each Paralympic athlete is shown in Appendix 3.3. The measurements are presented as arithmetic means across consecutive DXA scans with uncertainties expressed as ± 1 standard deviation. The lengths represent the linear distances between the proximal and distal endpoints. The measurements had a high degree of test-retest reliability, as indicated by the small standard deviations. For Paralympian's A1-A6, the lengths differed by approximately 3.4 % ± 3.1 pp between parallel body segments in the right and left extremities. Similar inter- and intra-subject asymmetrical differences were previously reported for able-bodied individuals (Clauser et al, 1969; Dempster, 1955).

Appendix 3.3. The length (m) of each body segment for each Paralympic athlete.

Segment	A1	A2	A3	A4	A5	A6
H&N	0.250 ± 0.009	0.249 ± 0.001	0.274 ± 0.003	0.265 ± 0.001	0.265 ± 0.005	0.304 ± 0.005
TOR	0.599 ± 0.015	0.563 ± 0.002	0.649 ± 0.002	0.567 ± 0.001	0.588 ± 0.008	0.525 ± 0.022
UAR	0.283 ± 0.001	0.256 ± 0.007	0.311 ± 0.020	0.280 ± 0.004	0.291 ± 0.005	0.298 ± 0.001
UAL	0.284 ± 0.009	0.255 ± 0.012	0.320 ± 0.002	0.275 ± 0.001	0.290 ± 0.001	0.304 ± 0.001
FAR	0.236 ± 0.003	0.222 ± 0.001	0.271 ± 0.010	0.226 ± 0.001	0.276 ± 0.002	0.273 ± 0.002
FAL	0.228 ± 0.002	0.224 ± 0.001	0.267 ± 0.004	0.216 ± 0.001	0.280 ± 0.007	0.260 ± 0.001
HDR	0.156 ± 0.007	0.165 ± 0.001	0.192 ± 0.012	0.165 ± 0.002	0.123 ± 0.001	0.178 ± 0.009
HDL	0.145 ± 0.020	0.170 ± 0.004	0.182 ± 0.007	0.169 ± 0.003	0.117 ± 0.002	0.180 ± 0.006
THR	0.397 ± 0.011	0.372 ± 0.017	0.406 ± 0.010	0.369 ± 0.001	0.469 ± 0.003	0.413 ± 0.007
THL	0.250 ± 0.011	0.379 ± 0.008	0.411 ± 0.001	0.362 ± 0.001	0.464 ± 0.004	0.459 ± 0.001
SHR	0.339 ± 0.004	0.335 ± 0.001	0.424 ± 0.004	0.337 ± 0.003	0.398 ± 0.001	0.373 ± 0.008
SHL	N/A ± N/A	0.332 ± 0.001	0.423 ± 0.014	0.346 ± 0.005	0.400 ± 0.001	0.409 ± 0.003
FTR	0.187 ± 0.001	0.164 ± 0.003	0.174 ± 0.019	0.156 ± 0.008	0.178 ± 0.003	0.193 ± 0.002
FTL	N/A ± N/A	0.157 ± 0.001	0.161 ± 0.009	0.155 ± 0.005	0.187 ± 0.003	0.193 ± 0.001

Appendix 3.4 presents the mass of each body segment for each Paralympic athlete as experimentally measured via the DXA imaging. For Paralympian's A1-A6, the mass differed by approximately 5.4 % ± 4.6 pp between the corresponding body segments in the right and left extremities. The mass measurements had a high degree of test-retest reliability, as evidenced by the minor uncertainties. Summing the mass of each body segment for each Paralympic athlete resulted in estimated total body masses: A1 = 80.25 ± 0.10 kg, A2 = 64.21 ± 0.14 kg, A3 = 116.23 ± 0.30 kg, A4 = 72.96 ± 0.08 kg, A5 = 87.21 ± 0.96 kg, and A6 = 54.76 ± 0.18 kg.

Appendix 3.4. The mass (kg) of each body segment for each Paralympic athlete.

Segment	A1	A2	A3	A4	A5	A6
H&N	6.361 ± 0.248	5.990 ± 0.062	8.425 ± 0.295	6.137 ± 0.010	6.967 ± 0.085	6.496 ± 0.127
TOR	46.50 ± 0.011	34.79 ± 0.185	65.54 ± 1.188	37.16 ± 0.235	44.62 ± 0.677	24.57 ± 0.445
UAR	3.521 ± 0.173	2.533 ± 0.017	3.799 ± 0.381	3.319 ± 0.012	3.099 ± 0.192	2.431 ± 0.035
UAL	3.494 ± 0.250	2.480 ± 0.083	3.832 ± 0.525	2.887 ± 0.173	3.100 ± 0.035	2.357 ± 0.087
FAR	1.395 ± 0.023	1.135 ± 0.016	1.721 ± 0.074	1.057 ± 0.025	1.371 ± 0.009	1.104 ± 0.007
FAL	1.338 ± 0.028	1.173 ± 0.018	1.560 ± 0.064	0.995 ± 0.005	1.302 ± 0.027	1.042 ± 0.005
HDR	0.496 ± 0.008	0.419 ± 0.001	0.598 ± 0.013	0.322 ± 0.003	0.396 ± 0.011	0.370 ± 0.021
HDL	0.509 ± 0.008	0.422 ± 0.006	0.617 ± 0.004	0.323 ± 0.001	0.437 ± 0.013	0.375 ± 0.032
THR	8.090 ± 0.144	4.663 ± 0.062	9.326 ± 0.187	6.456 ± 0.097	8.383 ± 0.629	4.609 ± 0.247
THL	4.047 ± 0.030	4.968 ± 0.069	9.526 ± 0.387	7.093 ± 0.074	9.396 ± 0.201	4.938 ± 0.078
SHR	3.408 ± 0.057	2.011 ± 0.006	4.525 ± 0.073	2.852 ± 0.091	3.482 ± 0.034	2.393 ± 0.003
SHL	N/A ± N/A	2.033 ± 0.004	4.160 ± 0.081	2.821 ± 0.098	3.261 ± 0.071	2.336 ± 0.016
FTR	1.097 ± 0.013	0.798 ± 0.009	1.313 ± 0.070	0.795 ± 0.017	1.039 ± 0.008	0.934 ± 0.015
FTL	N/A ± N/A	0.790 ± 0.012	1.292 ± 0.026	0.745 ± 0.044	1.037 ± 0.039	0.944 ± 0.011

There is currently insufficient evidence to suggest that the position vector of the center of mass and the principal mass moment of inertia of a given body segment significantly differ between manual wheelchair users and able-bodied matched controls. Accordingly, the position vector of the center of mass from the proximal endpoint and the principal mass moment of inertia about the center of mass of each body segment for each Paralympic athlete was mathematically approximated via equations (2) and (3) respectively; the results are presented in Appendix 3.5 and 3.6.

Appendix 3.5. The position vector of the center of mass (m) of each body segment for each Paralympic athlete as computed via equation (2).

Segment	A1	A2	A3	A4	A5	A6
H&N	0.116 ± 0.004	0.116 ± 0.004	0.127 ± 0.001	0.123 ± 0.001	0.123 ± 0.003	0.141 ± 0.002
TOR	0.228 ± 0.006	0.214 ± 0.007	0.247 ± 0.001	0.216 ± 0.001	0.224 ± 0.003	0.200 ± 0.008
UAR	0.145 ± 0.001	0.131 ± 0.004	0.159 ± 0.010	0.143 ± 0.002	0.149 ± 0.002	0.153 ± 0.001
UAL	0.145 ± 0.004	0.131 ± 0.006	0.164 ± 0.001	0.141 ± 0.001	0.149 ± 0.001	0.156 ± 0.001
FAR	0.092 ± 0.001	0.086 ± 0.001	0.105 ± 0.004	0.088 ± 0.001	0.108 ± 0.001	0.106 ± 0.002
FAL	0.089 ± 0.001	0.087 ± 0.004	0.104 ± 0.002	0.084 ± 0.001	0.109 ± 0.003	0.101 ± 0.001
HDR	0.028 ± 0.001	0.030 ± 0.001	0.035 ± 0.002	0.030 ± 0.001	0.022 ± 0.001	0.032 ± 0.002
HDL	0.026 ± 0.004	0.031 ± 0.001	0.033 ± 0.001	0.031 ± 0.001	0.021 ± 0.001	0.032 ± 0.001
THR	0.148 ± 0.004	0.139 ± 0.006	0.151 ± 0.004	0.137 ± 0.001	0.174 ± 0.001	0.154 ± 0.002
THL	N/A ± N/A	0.141 ± 0.003	0.153 ± 0.001	0.135 ± 0.001	0.173 ± 0.002	0.171 ± 0.001
SHR	0.126 ± 0.001	0.124 ± 0.002	0.157 ± 0.002	0.125 ± 0.002	0.147 ± 0.001	0.138 ± 0.003
SHL	N/A ± N/A	0.123 ± 0.004	0.157 ± 0.005	0.128 ± 0.003	0.148 ± 0.001	0.152 ± 0.001
FTR	0.084 ± 0.001	0.074 ± 0.002	0.078 ± 0.008	0.070 ± 0.004	0.082 ± 0.002	0.086 ± 0.001
FTL	N/A ± N/A	0.070 ± 0.001	0.072 ± 0.004	0.069 ± 0.002	0.087 ± 0.002	0.087 ± 0.001

Appendix 3.6. The principal mass moment of inertia (kg·$\mathbf{m^2}$) about the center of mass of each body segment for each Paralympic athlete as calculated via equation (3).

Segment	A1	A2	A3	A4	A5	A6
H&N	0.159 ± 0.018	0.149 ± 0.003	0.253 ± 0.015	0.172 ± 0.001	0.196 ± 0.010	0.240 ± 0.013
TOR	3.087 ± 0.152	2.040 ± 0.002	5.102 ± 0.129	2.208 ± 0.012	2.851 ± 0.035	1.251 ± 0.082
UAR	0.026 ± 0.001	0.015 ± 0.001	0.034 ± 0.008	0.024 ± 0.001	0.024 ± 0.002	0.020 ± 0.001
UAL	0.026 ± 0.003	0.015 ± 0.002	0.036 ± 0.004	0.020 ± 0.001	0.024 ± 0.001	0.020 ± 0.001
FAR	0.008 ± 0.001	0.006 ± 0.001	0.013 ± 0.001	0.005 ± 0.001	0.012 ± 0.001	0.008 ± 0.001
FAL	0.007 ± 0.001	0.006 ± 0.001	0.011 ± 0.001	0.005 ± 0.001	0.010 ± 0.001	0.007 ± 0.001
HDR	0.004 ± 0.001	0.004 ± 0.001	0.008 ± 0.001	0.003 ± 0.001	0.002 ± 0.001	0.004 ± 0.001
HDL	0.004 ± 0.002	0.004 ± 0.002	0.007 ± 0.001	0.003 ± 0.001	0.002 ± 0.001	0.004 ± 0.001
THR	0.154 ± 0.012	0.078 ± 0.008	0.186 ± 0.005	0.106 ± 0.002	0.223 ± 0.014	0.095 ± 0.008
THL	N/A ± N/A	0.086 ± 0.005	0.195 ± 0.009	0.112 ± 0.002	0.244 ± 0.009	0.126 ± 0.003
SHR	0.050 ± 0.002	0.029 ± 0.002	0.103 ± 0.004	0.041 ± 0.002	0.070 ± 0.001	0.042 ± 0.002
SHL	NA ± NA	0.029 ± 0.002	0.095 ± 0.008	0.043 ± 0.001	0.066 ± 0.002	0.050 ± 0.001
FTR	0.007 ± 0.001	0.004 ± 0.002	0.007 ± 0.002	0.004 ± 0.001	0.006 ± 0.001	0.006 ± 0.001
FTL	NA ± NA	0.004 ± 0.001	0.006 ± 0.001	0.003 ± 0.001	0.007 ± 0.001	0.006 ± 0.001

For Paralympian's A1–A6, the mass of each body segment as a percentage of the Paralympian's total body mass as determined via the DXA imaging were compared with the cadaveric approximations by Clauser et al (1969) and Dempster (1955). The results are presented in Appendix 3.7 and 3.8, and represent percent differences between the DXA measurements and cadaveric approximations. The uncertainties denote inter-athlete differences. Negative quantities indicate that the cadaveric approximations were less than the experimental DXA measurements, and vice versa for positive quantities.

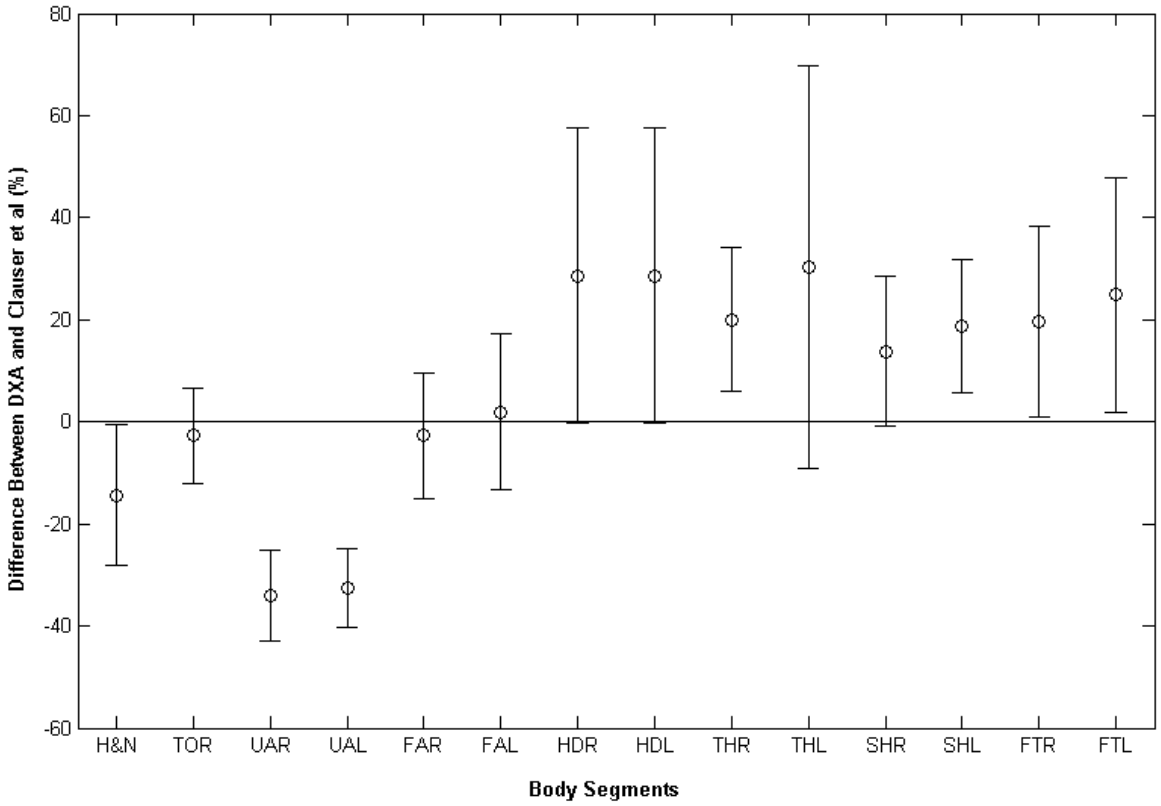

Appendix 3.7. Percent differences (%) in the mass percentages of each body segment between the DXA measurements and approximations by Clauser et al (1969).

Compared with the mass percentages from the DXA imaging, the cadaveric approximations were approximately 14.7 % ± 17.1 pp lower for the upper extremity body segments (i.e., head-and-neck, torso, upper arms, and forearms) and 18.5 % ± 15.8 pp higher for those in the lower extremities (i.e., thighs, shanks, and feet). The observed differences between the DXA measurements and cadaveric approximations support the implementation of the proposed database for developing valid multibody biomechanical models of Paralympic athletes.

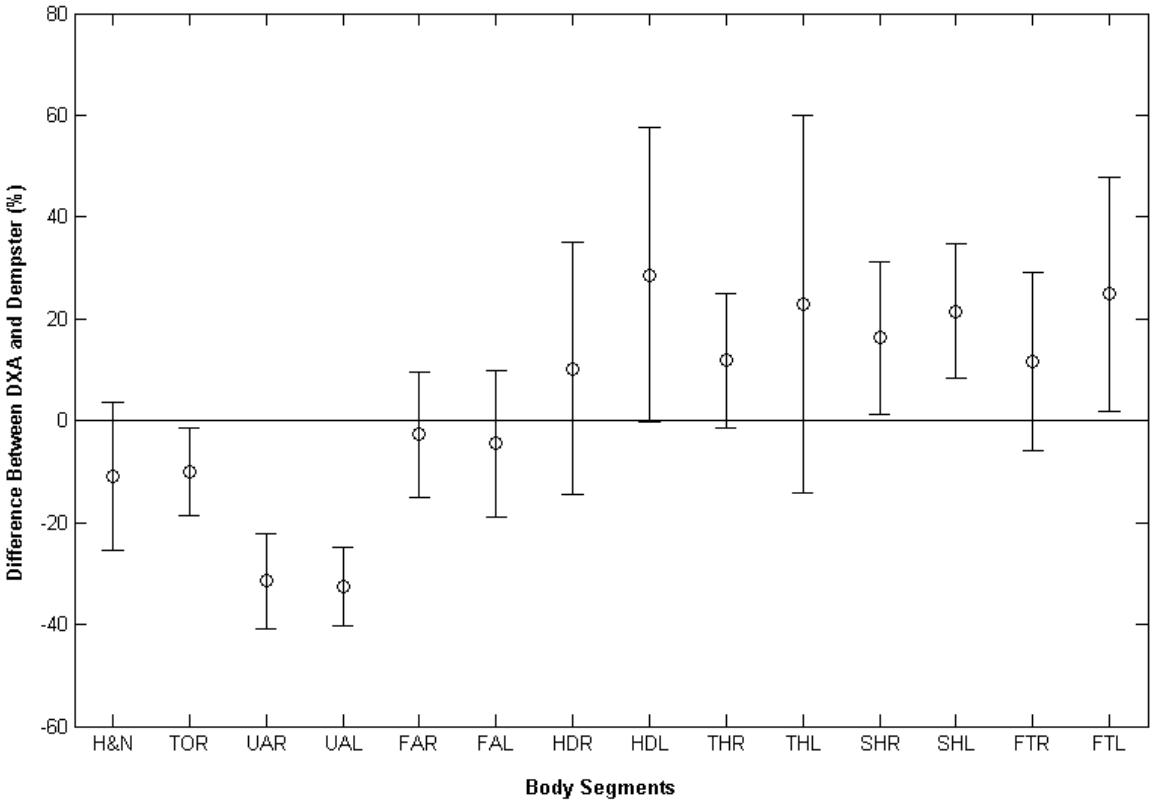

Appendix 3.8. Percent differences (%) in the mass percentages of each body segment between the DXA measurements and approximations by Dempster (1955).